Atmósfera 38, 829-862 (2024)
https://doi.org/10.20937/ATM.53367

Why did numerical weather forecasting systems fail to predict the Hurricane Otis's development?

Juan Carlos GUILLERMO-MONTIEL[1]*, Benjamín MARTÍNEZ-LÓPEZ[2], Carlos Abraham OCHOA-MOYA[2], Ignacio Arturo QUINTANAR[2] and William David CABOS-NARVÁEZ[3]

[1] *Posgrado en Ciencias de la Tierra, Universidad Nacional Autónoma de México, Circuito de la Investigación Científica s/n, Ciudad Universitaria, 04510 Ciudad de México, México.*
[2] *Instituto de Ciencias de la Atmósfera y Cambio Climático, Universidad Nacional Autónoma de México, Circuito de la Investigación Científica s/n, Ciudad Universitaria, 04510 Ciudad de México, México.*
[3] *Universidad de Alcalá, Alcalá de Henares, Madrid, España.*
*Corresponding author: jcarlosgm@atmosfera.unam.mx

Received: December 31, 2023; Accepted: May 31, 2024

RESUMEN

El huracán Otis (HO) ocurrió en el Pacífico tropical oriental (PTO), intensificándose rápida e inesperadamente, y tocó tierra cerca de Acapulco a las 06:25 UTC del 25 de octubre de 2023 como huracán categoría cinco. Los pronósticos meteorológicos nacionales (PMN), tanto el oficial como los no oficiales, fallaron en la predicción del desarrollo, la trayectoria y la intensificación del HO. Para analizar las razones que causaron este fallo de los PMN, realizamos dos experimentos utilizando el modelo Weather Research and Forecasting (WRF), con datos del Global Forecast System (GFS) y la quinta generación del reanálisis atmosférico del ECMWF (ERA5) como condición inicial (CI). Nuestros resultados mostraron que algunos campos del GFS, como humedad relativa, energía potencial convectiva disponible e incluso la temperatura superficial del mar fueron más favorables para el desarrollo y la intensificación de la perturbación en comparación con ERA5. Sin embargo, la estructura tridimensional del campo de viento en el PTO del GFS no contribuyó al desarrollo inicial del HO. Además, exploramos la sensibilidad del WRF a diferentes configuraciones del modelo para simular la trayectoria y la intensidad del huracán utilizando un sistema acoplado océano-atmósfera compuesto por el WRF y un modelo tridimensional de circulación del océano basado en Price-Weller-Pinkel. Nuestros experimentos numéricos implican modificaciones en la CI, parametrizaciones de cumulus (PC), coeficientes de rugosidad, resoluciones espaciales, diferentes pasos de tiempo y un modelo acoplado idealizado. Las pruebas de sensibilidad revelan la importancia del esquema de PC, donde el Kain-Fritsch fue el único que ayudó a simular el HO adecuadamente, así como el incremento de la resolución espacial. Además, el acoplamiento océano-atmósfera mejora la predicción del tiempo de llegada a tierra y la ubicación del HO. A pesar de esto, ningún experimento capturó la intensidad o la rápida intensificación del HO.

ABSTRACT

Hurricane Otis (HO) occurred in the eastern tropical Pacific (ETP), intensifying rapidly and unexpectedly, making landfall near Acapulco at 06:25 UTC on October 25, 2023 as a category five hurricane. Official and unofficial national weather forecasts (NWF) failed to predict HO's development, trajectory, and intensification. To analyze the reasons for the failure of the NWF, we conducted two experiments using the Weather Research and Forecasting (WRF) model, with Global Forecast System (GFS) and fifth-generation ECMWF atmospheric reanalysis (ERA5) data as initial condition (IC). Our results showed that some fields in the GFS data, such as relative humidity, convective available potential energy, and even sea surface temperature, were more favorable for the development and intensification of the disturbance compared to ERA5. However, the three-dimensional structure of the wind field in the ETP in GFS did not contribute to the initial development of HO. Additionally, we explored the WRF's sensitivity to different model configurations to simulate the trajectory and intensity of the hurricane using a coupled ocean-atmosphere system composed of WRF and a three-dimensional upper-ocean circulation model based on Price-Weller-Pinkel. Our numerical experiments involve modifications in the IC, cumulus parameterizations (CP), roughness coefficients, spatial resolutions, different time steps, and an idealized coupled model. The sensitivity test reveals the significance of the CP scheme, where the Kain-Fritsch was the only one that helped simulate the HO properly, altogether with increased spatial resolution. Furthermore, ocean-atmosphere coupling improves the prediction of the landfall time and location of the HO. However, no experiment captured the intensity or rapid intensification of HO.

Keywords: Hurricane Otis development, initial condition, ERA5 reanalysis, cumulus parameterization scheme, coupled ocean-atmosphere system, WRF-PWP.

1. Introduction

Tropical cyclones (TC) are atmospheric phenomena that form over the ocean. Depending on their category, determined by the conditions of their development and evolution, they can exhibit high destructive power due to intense winds and heavy precipitation, leading to floods, landslides, and storm surges (Emanuel, 2003; Samala et al., 2013). The primary impacts of TC occur in coastal regions; however, depending on the specific conditions of each event, they could go further into the land, magnifying the damage. These phenomena affect the population through property loss and, quite often, human casualties. The damage to public infrastructure hinders access to essential services, creating unsanitary conditions in the affected areas and increasing the risk to public health. Due to its geographical location, Mexico is vulnerable to the impact of these phenomena, whether they originate from the Atlantic Ocean and the Caribbean Sea or the Pacific Ocean.

The lifespan of a TC, from genesis to dissipation, is on the order of hours to days. Consequently, it is paramount to have an accurate and timely forecast of this evolution in both trajectory and intensity, to adopt appropriate measures to save the integrity of the population and limit potential impacts. Numerical weather prediction (NWP) models, capable of simulating realistic scenarios of extreme atmospheric phenomena, are becoming a crucial tool in atmospheric sciences for decision-making and protection of the general population. The Weather Research and Forecasting model (WRF; Skamarock et al., 2008) is the most widely used among these models, serving scientific purposes and regional operational meteorological forecasting.

The role of the ocean in the time evolution of a TC is crucial since turbulent surface heat, momentum fluxes, and variations in sea surface temperature (SST) mediate the interaction between the ocean and the atmosphere across several time scales (Dorman et al., 2006). Indeed, tropical cyclogenesis and its fully developed form into a TC results from these mass, heat, and momentum exchanges across the ocean-atmosphere interface. Heat and moisture fluxes influence the intensification of a TC (Bruyère et al., 2012), while the SST field modulates its trajectory (Katsube and Inatsu, 2016). Therefore, it is essential to estimate these fluxes accurately in the simulation of such phenomena (Emanuel, 1995), requiring the inclusion of an active ocean component.

Ideally, three-dimensional models for ocean and atmosphere components are necessary for coupled ocean-atmosphere simulations, as demonstrated by various articles in the literature. For instance, Trent (2007) uses a one-dimensional mixing layer model (Price et al., 1986) coupled with WRF to simulate Hurricane Katrina (2005). The study concluded that a one-dimensional model cannot adequately represent the coupled system, recommending the analysis of this effect with three-dimensional models. Mooney et al. (2016) analyzed Hurricane Irene (2011) using an atmospheric model coupled to a one-dimensional mixing layer model based on Pollard et al. (1973). The coupling to the Regional Ocean Modelling System model (ROMS; Shchepetkin and McWilliams, 2005; Haidvogel et al., 2008) resulted in a closer performance to what was observed immediately after the hurricane's passage, while the one-dimensional model did not properly represent the ocean recovery towards the conditions before the hurricane's passage.

In this context, it is essential to mention that using a fully three-dimensional coupled ocean-atmosphere model is not trivial because of its high computational cost and complexity in fine-tuning and maintaining. Therefore, it is customary to run the WRF model in atmospheric mode by simply prescribing the SST field and omitting the coupling to a full-fledged ocean model. An alternative is to couple WRF to a mixed-layer ocean model with different thermodynamic and dynamic approximation degrees. Thus, cheaper and more realistic simulations from the atmospheric mode option can be obtained by carefully selecting the physical parameterizations that best represent the atmosphere-ocean interactions.

An important WRF feature is its wide range of parameterizations representing physical processes. Currently, numerous studies focus on analyzing the sensitivity of the WRF to changes in its configuration. For example, how the model skill increases (or decreases) using a combination of different schemes for microphysics, cumulus, radiation, and planetary boundary layer; how the model performance is affected by using different data in the initial conditions, different horizontal and vertical resolution, as well using nesting (e.g., Gbode et al., 2019; Sun and Bi, 2019; Varga and Breuer, 2020; Singh et al., 2021; Aquino-Martínez et al., 2023).

The representation of clouds, convection, and the associated radiative properties are crucial in determining the atmosphere's evolution on different time scales. The processes occurring with clouds result in nonlinear effects on atmospheric circulation. Therefore, the choice of a cumulus convection scheme will impact not only the hydrological cycle but also the large-scale flows due to the release of latent heat and the vertical transport of momentum, sensible heat, and water vapor (e.g., Yao and del Genio, 1999; Arakawa, 2004; Yang et al., 2015).

Several authors analyze the performance of different cumulus convection parameterizations in the evolution of tropical cyclone studies (Davis et al. [2010], Chandrasekar and Bajali [2012], Torn and Davis [2012], Biswas et al. [2014]). Among the various cumulus parameterizations employed, Kain-Fritsch (Kain, 2004) and Tiedkte (Tiedkte, 1989; Zhang et al., 2011) stood out, showing the best results in trajectories and intensity.

At this moment, it is impossible to establish a specific WRF parameterization configuration as the best set, given that atmospheric characteristics vary according to the specific features of the region of interest and the type of phenomenon to analyze. Therefore, it is necessary to run some tests to find the configuration that better represents our case study.

Here we analyze the case of Hurricane Otis (HO), which rapidly and unexpectedly made landfall near Acapulco City as a category five hurricane. In the days leading up to the landfall, the operational available national weather forecast (NWF), including the official NWF issued by the Servicio Meteorológico Nacional (SMN) and the unofficial NWF issued by Instituto de Ciencias de la Atmósfera y Cambio Climático (ICAyCC), failed in predicting the HO trajectory and intensification. Forecasts kept simulating the system (HO) over the ocean for several days with no displacement towards the coast. This issue was present in the forecast initialized at 00:00 UTC on October 23 and 24, 2023. The true nature of HO and its potential danger only became apparent when a Hurricane Hunter aircraft flight (only one flight) conducted two eye penetrations into the hurricane at 19:00 and 20:00 UTC on October 24. The actual intensity far exceeded the estimates derived from satellite image analysis.

This study aims to analyze the reason(s) for the failure of official and unofficial NWFs (SMN and ICAyCC). Both forecasts use the Global Forecast System (GFS) as the initial condition (IC). Thus, we used WRF with GFS as the IC in an initial exploratory analysis. As expected, our simulation did not adequately simulate HO in agreement with SMN and ICAyCC. Afterwards, we replicate the experiment using information from the fifth generation of the ECMWF atmospheric reanalysis (ERA5) for the IC. Our goal in using ERA5 is not to compare the skills of these different databases since clearly, ERA5 represents a better atmospheric state due to its greater data assimilation window, and, precisely, that is our goal. If ERA5 as an IC performs well in simulating HO, we can analyze its better atmospheric state representation than that from GFS to understand the deficiencies of GFS in representing the initial atmospheric structure that led to the local forecast failure. In addition to the IC, other essential fields in developing storms and tropical cyclones were analyzed, such as the environmental steering flow, relative humidity (RH), convective available potential energy (CAPE), relative vorticity (RV), and kinetic energy (KE). The analysis of the IC revealed that the three-dimensional wind field structure of GFS in the eastern tropical Pacific did not contribute to the initial development of Otis. Despite the RH and CAPE being more favorable for the disturbance's intensification than ERA5, the strong vertical wind shear from GFS inhibited the initial development of the perturbation.

Once we get the HO development by using ERA5 as an IC, we explore the WRF sensitivity to different model configurations to simulate the trajectory and intensity of the hurricane, choosing the best model configuration. With this best model configuration for the WRF, we additionally use a coupled ocean-atmosphere system composed of the WRF model and a three-dimensional upper-ocean circulation model to estimate the effect on the simulation of an active idealized ocean. Our numerical experiments involve modifications in initial conditions, cumulus parameterizations, roughness coefficients, spatial resolutions, different time steps, and an idealized coupled model. These model's sensitivity tests represent the first approach to an appropriate setup for simulating tropical cyclones in the eastern tropical Pacific, including the ocean effect. Sensitivity tests show that including ocean-atmosphere coupling reduces the error in landfall, although no experiment captured intensity or rapid intensification.

We organize the work as follows: Section 2 describes Hurricane Otis; Section 3 describes the numerical system used, including details about datasets, the numerical experiments designs, and the applied methods; Section 4 presents the results, and Section 5 includes discussion and conclusions.

2. Case study: Hurricane Otis

Hurricane Otis occurred in the eastern region of the Pacific Ocean from October 22 to 25, 2023. According to the US National Hurricane Center (NHC), HO was the strongest hurricane to land in the Eastern Pacific. The effects caused by the impact of HO are categorized as catastrophic in all aspects, destroying or severely damaging the city's infrastructure: public services, energy, telecommunications, commercial, and land transportation routes. Additionally, there was partial or total destruction of homes and buildings, along with the unfortunate loss of human lives. In the following days, Acapulco faced a humanitarian crisis.

Based on the update from Public Advisory (PA) 12A of the NHC (NHC, 2023), HO made landfall near the city of Acapulco in the Mexican state of Guerrero at 06:25 UTC (00:25 LT) on October 25, 2023, as a category five hurricane on the Saffir-Simpson Hurricane Wind Scale, with estimated maximum sustained winds of 270 km h^{-1} and a minimum central pressure of 923 hPa. Going back in time, according to PA3 issued by the NHC at 03:00 UTC on October 23, 2023, the forecast indicated that HO would make landfall on the coasts of Guerrero as a tropical storm, as shown in Figure 1. However HO intensified unexpectedly, transitioning from a tropical storm at 15:00 UTC on October 24 (PA9) to a category five hurricane at 03:00 UTC on October 25 (PA12), a period of approximately 12 h.

3. Data and methods

3.1 Description of the coupled system

The numerical simulation system used in this study is the WRF-PWP, a coupled ocean-atmosphere system. The WRF-PWP components are described below.

3.1.1 Atmospheric component

The atmospheric model used in this study is the Advanced Research WRF, the dynamical core of the WRF (Skamarock et al., 2008) v. 3.8.1. The WRF model is a state-of-the-art mesoscale weather prediction system designed for atmospheric research and operational forecasting applications. It is a non-hydrostatic model with Eulerian-type equations, solved on an Arakawa C-grid in the horizontal and terrain-following hydrostatic pressure as a vertical coordinate system. The model offers various options for physical parameterizations, including microphysics processes, cumulus convection, planetary boundary layer, surface layer, land surface energy exchange, and radiation transfer (both longwave and shortwave).

3.1.2 Oceanic component

We use the Price-Weller-Pinkel (PWP; Price et al., 1986, 1994; Lee and Chen, 2014) model for the oceanic component. PWP is a three-dimensional hydrostatic and time-dependent upper-ocean circulation

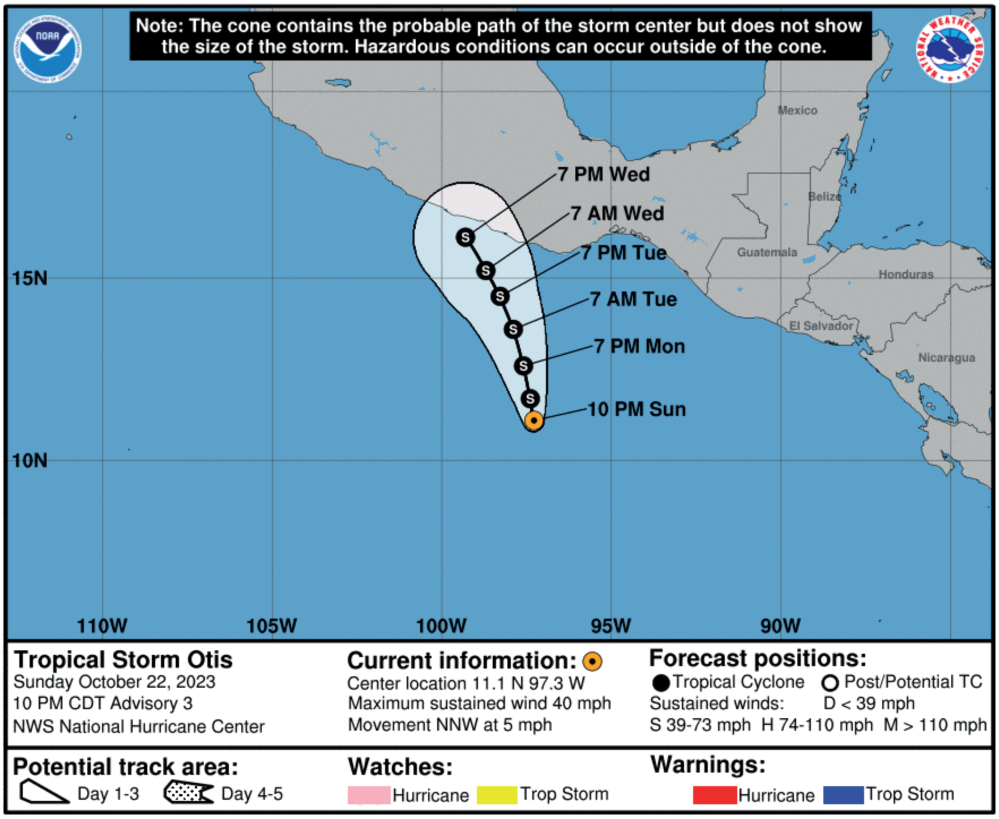

Fig. 1. NHC forecast for tropical storm Otis at 03:00 UTC on October 23, 2023 (source: NHC).

model incorporated in the WRF that simulates processes in the upper ocean resulting from interactions among the complex atmosphere and the simplified ocean equations of momentum, temperature, and salinity.

$$\frac{\partial \boldsymbol{V}}{\partial t} + \boldsymbol{f K} \times \boldsymbol{V} + \boldsymbol{V} \cdot \nabla \boldsymbol{V} + \boldsymbol{W} \frac{\partial \boldsymbol{V}}{\partial z} = \frac{1}{\rho_0} \frac{\partial \boldsymbol{\tau}}{\partial z} - \frac{1}{\rho_0} \nabla \boldsymbol{P} \tag{1}$$

$$\frac{\partial T}{\partial t} + V \cdot \nabla T + W \frac{\partial T}{\partial z} = \frac{1}{\rho_0 C_p} \frac{\partial H}{\partial z} \tag{2}$$

$$\frac{\partial \boldsymbol{S}}{\partial t} + \boldsymbol{V} \cdot \nabla \boldsymbol{S} + \boldsymbol{W} \frac{\partial \boldsymbol{S}}{\partial z} = \frac{\partial \boldsymbol{E}}{\partial z} \tag{3}$$

where V and ∇ are the horizontal current and gradient operator; $\boldsymbol{W}$ is the vertical component of velocity; $\boldsymbol{H}$, $\boldsymbol{E}$ and $\boldsymbol{\tau}$ are the heat, salinity, and momentum fluxes respectively; $\boldsymbol{T}$ and $\boldsymbol{S}$ are the temperature and salinity; $\boldsymbol{P}$ is the hydrostatic pressure; and $\boldsymbol{f}$ is the Coriolis parameter. A detailed description of the PWP model can be reviewed in Price et al. (1986, 1994).

3.2 Databases

The GFS (NCEP, 2015) is a weather forecast model from the National Centers for Environmental Prediction (NCEP) that generates data for dozens of atmospheric and land-soil variables, including temperature, wind, precipitation, soil moisture, and atmospheric ozone concentration. GFS couples four models (atmosphere, ocean, land/soil, and sea ice) accurately depicting weather conditions. Notice that GFS is forced with information from the Global Data Assimilation System (GDAS) of the National Centers for Environmental Information (NCEI), which assimilates data from various sources such as weather stations, radiosondes, wind profilers, aircraft data, buoys, and radars. In Mexico, like in many countries, regional operational forecast systems use IC from GFS.

On the other hand, the fifth-generation atmospheric reanalysis of the ECMWF (ERA5) is a reanalysis database available from the Copernicus Climate Change Service (Hersbach et al., 2023). ERA5 is not constrained to issue timely forecasts and assimilates information from various global observation sources. Because ERA5 data has a 5-day lag concerning the current date, it has more time for data collection and assimilation. The newly available observations, combined with previous forecasts in an optimal way, produce the best estimate of the state of the atmosphere. In this context, the modeling community commonly uses the ERA5 database as the reference data.

The ocean reanalysis database ECCO2 (Menemenlis et al., 2005, 2008) utilizes the Massachusetts Institute of Technology General Circulation Model (MITgcm), with a comprehensive ocean configuration coupled to a sea ice model. ECCO2 employs a data assimilation system that integrates information from various observation sources and satellite data, constraining the model solution while satisfying the laws of physics and thermodynamics. This database provides information on the three-dimensional structure of the ocean, including variables such as temperature, salinity, and zonal and meridional components of velocity. ECCO2 data are available globally on a regular latitude-longitude grid of 0.25º, with 50 vertical levels distributed from 5 to 5906.25 m depth.

NOAA Daily Optimum Interpolation Sea Surface Temperature (OISST, commonly known as Reynolds SST) v. 2.1 (Reynolds et al., 2007; Banzon et al., 2016; Huang et al., 2021) is a long-term climate data record that incorporates observations from different platforms (satellites, ships, buoys, and Argo floats) into a regular global grid. The dataset is interpolated to fill gaps on the grid and create a spatially complete SST map. Satellite and ship observations are referenced to buoys to compensate for platform differences and sensor biases.

3.3 Numerical experiment design

First, we reviewed the technical details of the WRF model configuration used in simulating the operational forecast system at the SMN and the ICAyCC. Based on this review, we build a similar configuration regarding domain dimensions, spatial resolution, and physical parameterizations. Subsequently, we conducted a series of experiments to analyze the model's sensitivity to changes in its configuration, including variations in initial conditions data, spatial resolution, and physical parameterizations. In all experiments, we use the following physical parameterization schemes: YSU (Yonsei University Scheme; Hong et al., 2006) for the planetary boundary layer; WSM6 (WRF Single-Moment 6-Class; Hong and Lim, 2006) for microphysics; RRTM (Mlawer et al., 1997) for shortwave radiation; Dudhia (Dudhia, 1989) for longwave radiation; MM5 (Beljaars, 1995) for surface layer, and Noah (Tewari et al., 2004) in land surface.

The domain covers Mexico with a spatial resolution of 15 km (15KM; 406 × 245 grid points) on a Mercator projection (the extent of the domain can be seen in Fig. 2). Horizontally, it remained consistent in the coupled system. We discretized the atmosphere vertically with 40 levels up to 50 hPa. We analyzed the model's sensitivity to spatial resolution, using 10 km (10KM; 609 × 348 grid points) and 5 km (5KM; 1218 × 736 grid points) spatial resolutions while maintaining the same vertical configuration.

Additionally, we tested different cumulus parameterization (CP) schemes. Two of these schemes are non-scale-aware: Kain-Fritsch (KF; Kain, 2004) and Tiedkte (TK; Tiedtke, 1989; Zhang et al., 2011); and two are scale-aware: Grell-Freitas (GF; Grell and Freitas, 2014) and multi-scale Kain-Fritsch (MSKF; Zheng et al., 2016; Glotfelty et al., 2019). In the experiments at a 5 km spatial resolution, we configured an experiment without cumulus parameterization, employing only the microphysics scheme (WSM6). Regarding the KF scheme, calls to the cumulus routines were made every 5 min (CUDT5) and at each time step (CUDT0).

We also use two different parameterizations to represent the momentum and enthalpy exchange coefficients between the ocean and the atmosphere through the roughness coefficients. Green and Zhang (2012) state that these coefficients influence the hurricane's wind intensity. For this purpose, we used option 0 (based on Charnock [1955]) and option 2 (based on Brutsaert [1975] and Donelan et al. [2004]) for the corresponding parameter. This configuration is referred to as roughness parameterization (RP).

All simulations started at 00:00 UTC on October 23, 54 h before HO made landfall, and continued for 84 h with hourly outputs. In the first experiment (CTRL), we obtained the atmospheric initial

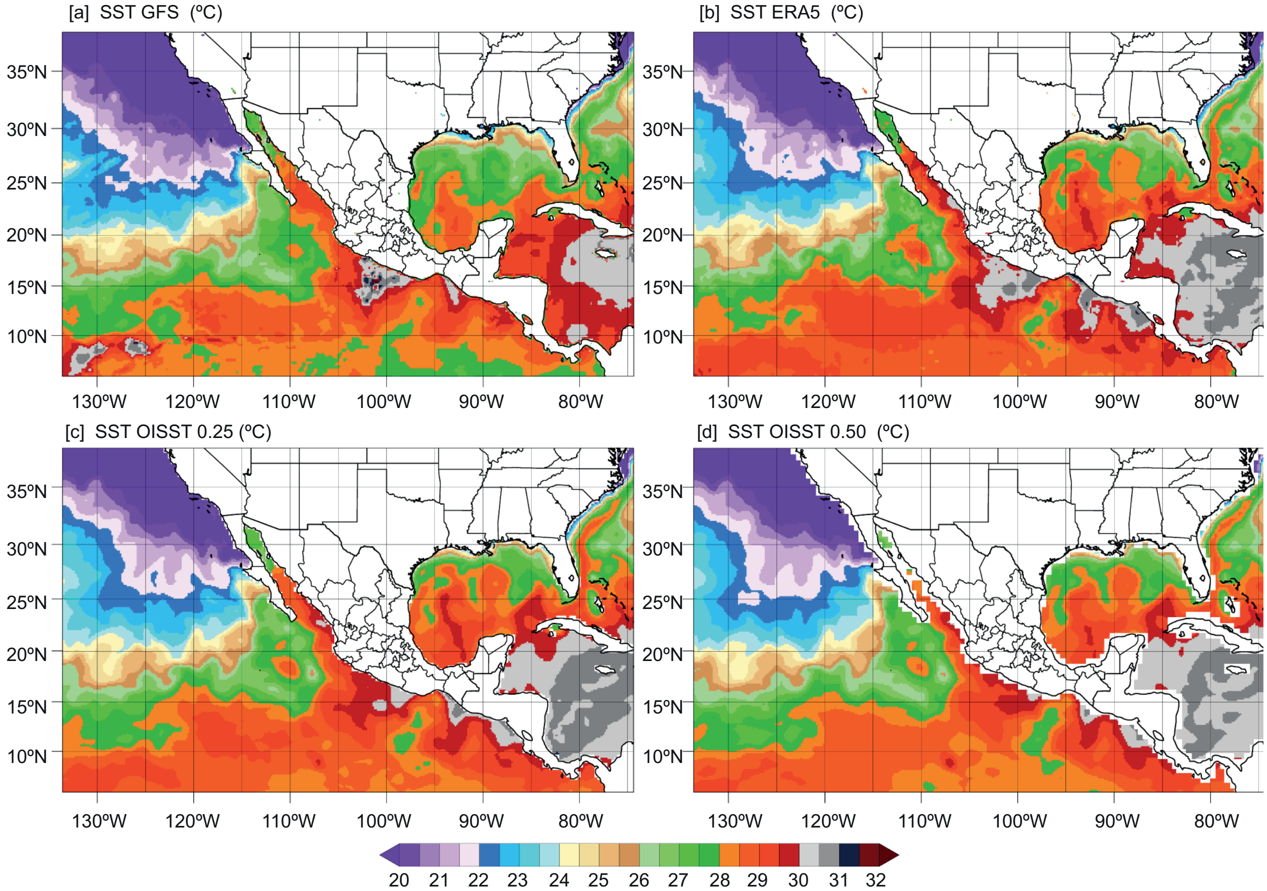

Fig. 2. Initial SST fields: (a) GFS at 00:00 UTC on October 23; (b) ERA5 at 00:00 UTC on October 23; (c) OISST 0.25 daily mean for October 23; (d) OISST 0.50 daily mean for October 23.

conditions (IC) and boundary conditions (BC) from the GFS at 0.25 resolution. Subsequently, we generated the IC and BC for all simulations using ERA5 at 0.25 resolution.

In the ATMOS experiments, we used WRF with prescribed SST fields from GFS and ERA5, which remain constant throughout the simulation. For experiments at a resolution of 15 km, we used time steps of 60 s; for experiments at a resolution of 10 km, we used time steps of 60 (DT60) and 30 s (DT30); in experiments at a resolution of 5 km, we used time steps of 15 s.

In the COUPLED experiments, we use the PWP model coupled to WRF. PWP automatically generates the three-dimensional initial field for temperature and salinity from surface fields of these variables and the corresponding vertical profiles obtained from ECCO2.

We analyze the model's sensitivity to different SST fields. In some experiments, we used the SST available in ERA5 as the surface field; in others, we use SST data from OISST at spatial resolutions of 0.25º and 0.50º. Note that in all COUPLED simulations, we use mean vertical profiles of temperature and salinity for October (mean values for 2018-2022) linearly interpolated to the depths set in PWP. The PWP model obtains the corresponding depth gradients of temperature from these profiles, adjusting the 3-D temperature fields for each SST field considered. For salinity, we use ECCO2 values at all levels. Figure 2 shows GFS, ERA5, OISST 0.25, and OISST 0.50 SST fields.

We also estimate the sensitivity of the model solution to changes in the ocean's vertical structure due to an increase in the mixed layer depth. To this aim, we prescribed the initial SST to the first 10 levels, homogenizing thus the temperature in the upper 100 m of the water column (HOM.T); we also prescribed temperature and salinity together, homogenizing thus the density in the HOM.TS. These additional experiments result from an analysis of the evolution of the 28º isotherm depth obtained from the operational ocean reanalysis ORAS5 (C3S, 2021), which shows a sustained increase of that depth during the last decades, implying an increase of available surface heat content in the upper waters of the eastern, northern tropical Pacific.

We conducted 33 numerical experiments, summarized in Table I. Notice that each experiment name relates to the employed configuration; the initial prefix determines whether it is a stand-alone atmospheric simulation (ATMOS) or a coupled one using WRF-PWP (COUPLED).

3.4 Methods

First, we identify HO's minimum mean sea level pressure (MSLP) value from each experiment, determining its geographical position based on each simulated trajectory. Then, we compare our results against the information available in the NHC-PA, determined as approximate values (at the time of writing, the official NHC report has yet to be available). For experiments simulating HO making landfall, landfall time, and simulated landfall MSLP were obtained, and the distance to the reported landfall point (LFP) was calculated. Based on the information mentioned earlier, the best results were determined by those showing the least time difference in landfall time and the shortest distance to the LFP. From the experiments determined as the best results, we obtain the simulated maximum wind speed (MWSP) values and compare them with available information in the PA. We group the results by experiment type (ATMOS and COUPLED) and spatial resolution. Maps present trajectories, while we show MSLP and MWSP in XY plots.

The environmental steering flow (ESF) is the spatially averaged ambient wind through a thickness of the atmospheric layer, starting from 850 hPa, which coincides with the TC's movement (Galarneau and Davis, 2012). The ESF analysis involves removing the wind field associated with the TC vortex (Neumann, 1979; Fiorino and Elsberry, 1989), which comprises contributions from synoptic-scale systems and asymmetric circulations induced by the TC itself (Holland, 1983; Fiorino and Elsberry, 1989; Wu and Emanuel, 1993).

Following Galarneau and Davis (2012), we calculated the ESF at each level between 850 and 250 hPa using 3º, 4º, and 5º radii from the simulated storm surface center in each experiment at 3-h intervals. Subsequently, for each radius, the ESF is obtained for five different atmospheric thicknesses: 850-750, 850-650, 850-500, 850-400, and 850-300 hPa. In a preliminary analysis, we determined that the ESF results are better with a radius of 3º. For simplicity, we keep the same radius for ESF calculations throughout the whole simulation.

Finally, we used the same radius to calculate the average RV, KE, RH, and CAPE values for each level between the surface and 300 hPa at 3-h intervals. We present these results in Hovmöller plots.

4. Results

The experiments fall into ATMOS and COUPLED categories, indicating whether WRF uses a prescribed SST field or the WRF-PWP is active, respectively. Each category has numerical experiments with 5, 10, and 15 km spatial resolutions. Additionally, we divided these categories into subcategories based on using specific configurations. All times that we use in the analysis are UTC. HO made landfall near Acapulco at 06:25 on October 25. Considering this, we conducted the analyses for a maximum of 66 h, corresponding to 18:00 on October 25 (12 h after HO made landfall).

4.1 Trajectories and mean sea level pressure

In Figures 3 to 11, the simulated trajectories are represented by lines of different colors, with each map indicating the corresponding color for each experiment. Markers (dots) over the trajectories indicate a specific time: black dots correspond to 00:00, and orange dots to noon. The black line corresponds to the trajectory of HO, according to the PA, and the numbers to its right indicate the date and time (DDHH format) of each position; the pink dot on this trajectory represents the location where HO made landfall; the star marker (with date/time 2419) corresponds to the position reported by the Hurricane Hunter aircraft flight. Note that simulated

Table I. Summary of the experiments, based on the different configurations used.

Experiment name	HR	Atmosphere					Ocean	
		IC	CP	RP	DT	CUDT	SST data	HOM
ATMOS_GFS_KF-0_15KM	15	GFS	KF	0	60	5	NA	NA
ATMOS_ERA5_GF-0_15KM	15	ERA5	GF	0	60	NA	NA	NA
ATMOS_ERA5_KF-0_15KM	15	ERA5	KF	0	60	5	NA	NA
ATMOS_ERA5_KF-2_15KM	15	ERA5	KF	2	60	5	NA	NA
ATMOS_ERA5_GF-0_10KM_DT30	10	ERA5	GF	0	60	NA	NA	NA
ATMOS_ERA5_KF-0_10KM_DT60_CUDT5	10	ERA5	KF	0	60	5	NA	NA
ATMOS_ERA5_KF-0_10KM_DT30_CUDT5	10	ERA5	KF	0	30	5	NA	NA
ATMOS_ERA5_KF-0_10KM_DT30_CUDT0	10	ERA5	KF	0	30	0	NA	NA
ATMOS_ERA5_KF-2_10KM_DT60_CUDT5	10	ERA5	KF	2	60	5	NA	NA
ATMOS_ERA5_KF-2_10KM_DT30_CUDT5	10	ERA5	KF	2	60	5	NA	NA
ATMOS_ERA5_KF-2_10KM_DT30_CUDT0	10	ERA5	KF	2	60	0	NA	NA
ATMOS_ERA5_TK-0_10KM_DT30	10	ERA5	TK	0	30	NA	NA	NA
ATMOS_ERA5_TK-2_10KM_DT30	10	ERA5	TK	2	30	NA	NA	NA
ATMOS_ERA5_MSKF-0_10KM_DT30	10	ERA5	MSKF	0	30	NA	NA	NA
ATMOS_ERA5_MSKF-2_10KM_DT30	10	ERA5	MSKF	2	30	NA	NA	NA
ATMOS_ERA5_KF-0_5KM_CUDT0	5	ERA5	KF	0	15	0	NA	NA
ATMOS_ERA5_WSM6-0_5KM	5	ERA5	NA	0	15	NA	NA	NA
ATMOS_ERA5_GF-0_5KM	5	ERA5	GF	0	15	NA	NA	NA
ATMOS_ERA5_MSKF-0_5KM	5	ERA5	MSKF	0	15	NA	NA	NA
COUPLED_ERA5_KF-0_15KM	15	ERA5	KF	0	60	5	ERA5	NA
COUPLED_ERA5_KF-0_15KM_HOM.T	15	ERA5	KF	0	60	5	ERA5	T
COUPLED_ERA5_KF-0_10KM_CUDT5	10	ERA5	KF	0	30	5	ERA5	NA
COUPLED_ERA5_KF-0_10KM_HOM.T_CUDT5	10	ERA5	KF	0	30	5	ERA5	T
COUPLED_ERA5_KF-0_10KM_HOM.TS_CUDT5	10	ERA5	KF	0	30	5	ERA5	T,S
COUPLED_ERA5_KF-0_10KM_HOM.TS_CUDT0	10	ERA5	KF	0	30	0	ERA5	T,S
COUPLED_OISST_0.50_KF-0_10KM_CUDT5	10	ERA5	KF	0	30	5	OISST 0.50	NA
COUPLED_OISST_0.50_KF-0_10KM_HOM.T_CUDT5	10	ERA5	KF	0	30	5	OISST 0.50	T
COUPLED_OISST_0.50_KF-0_10KM_HOM.TS_CUDT5	10	ERA5	KF	0	30	5	OISST 0.50	T,S
COUPLED_OISST_0.25_KF-0_10KM_CUDT5	10	ERA5	KF	0	30	5	OISST 0.25	NA
COUPLED_OISST_0.25_KF-0_10KM_HOM.TS_CUDT5	10	ERA5	KF	0	30	5	OISST 0.25	T,S
COUPLED_OISST_0.25_KF-0_10KM_HOM.TS_CUDT0	10	ERA5	KF	0	30	0	OISST 0.25	T,S
COUPLED_OISST_0.25_KF-2_10KM_HOM.TS_CUDT0	10	ERA5	KF	2	30	0	OISST 0.25	T,S
COUPLED_OISST_0.25_KF-0_5KM_HOM.TS_CUDT0	5	ERA5	KF	0	15	0	OISST 0.25	T,S

HR: horizontal resolution in km; IC: database for IC for the atmosphere; CP: cumulus parameterization scheme; RP: roughness parameterization option; DT: time step in seconds; CUDT: cumulus routine call time; SST data: database for SST in ocean IC; HOM: ocean homogenization (T: temperature, S: salinity); NA: does not apply.

trajectories start at 00:00 on October 23, while the reported trajectory starts at 03:00.

4.1.1 Experiments at a spatial resolution of 15 kilometers

Figure 3 shows the trajectories of HO. In the CTRL experiment, the simulated system showed a slow and erratic trajectory during the first 24 h, moving later towards the northwest-east while staying over the ocean and away from the coast. This behavior is consistent with the simulations from the SMN and ICAyCC for that date.

On the other hand, when we used the same parameterization configuration as in the CTRL experiment but using ERA5 as IC (ERA5-KF), these experiments simulated a trajectory toward the coast, almost parallel to the reported trajectory, making landfall to the northwest of Acapulco. Among these, the best

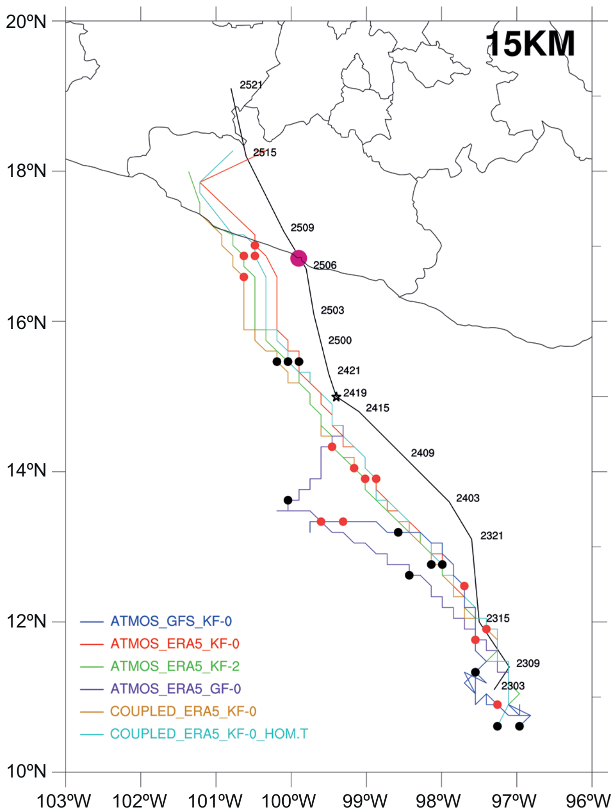

Fig. 3. Simulated trajectories of Hurricane Otis in 15KM experiments. Lines of different colors represent trajectories. The black line corresponds to the trajectory reported by NHC. Simulated trajectories start at 00:00 on October 23, while the reported trajectory starts at 03:00.

result corresponds to the simulated trajectory in ATMOS_ERA5_KF-0, which simulates landfall at 12:00 (+6H, 6 h after the actual time) at 64.84 km from the LFP, while ATMOS_ERA5_KF-2 makes landfall at +8H at 99.36 km. In contrast, the worst result corresponds to COUPLED_ERA5-KF0, making landfall at +11H at 114.1 km of the LFP; however, the COUPLED_ERA5_KF-0_HOM.T experiment improves considerably with results of +7H at a distance of 64.84 km (same distance as ATMOS_ERA5_KF-0).

ATMOS_ERA5_GF-0 simulated a system that remained over the ocean with an initial northwest displacement. It later changed direction towards the northeast without approaching land. Notice that the position reported by the Hurricane Hunter aircraft marks a significant change in the trajectory, with a nearly straight path toward the coast from that point onward.

Figure 4 shows the MSLP from experiments that made landfall. The colors associated with each experiment are consistent with Figure 3; black dots represent US National Hurricane Center (NHC) data, and the star marker corresponds to the value reported by the Hurricane Hunter flight at 19:00 on October 24.

All experiments follow the NHC-reported data very well in the first 12 h. Subsequently, all experiments show a gradual intensification reaching its maximum at 48 h (44 h in COUPLED_ERA5_

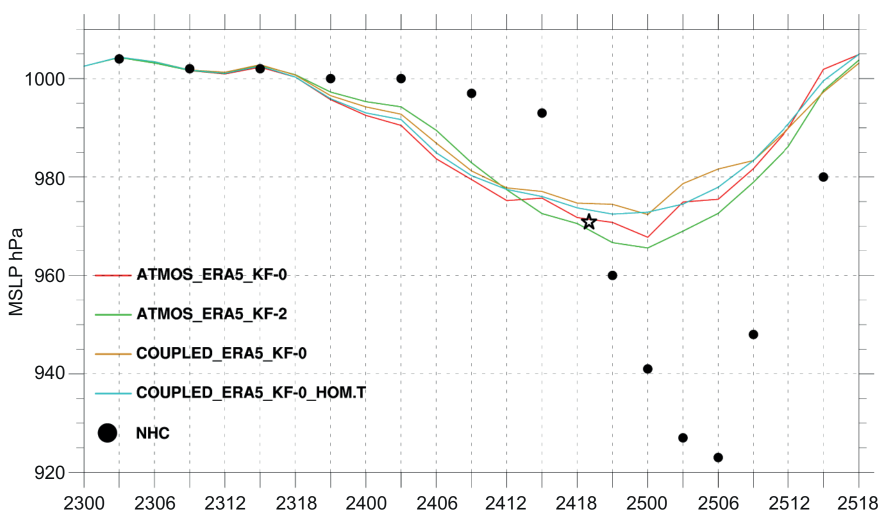

Fig. 4. Simulated MSLP of the experiments at 15KM that made landfall. The colors associated with each experiment are consistent with Figure 3. Black dots represent NHC data.

KF-0_HOM.T). ATMOS experiments show a lower MSLP than COUPLED, with the lowest MSLP of 965.58 hPa simulated in the ATMOS_ERA5_KF-2 experiment. In comparison, in the COUPLED experiment, the lowest MSLP of 971.4 hPa was in COUPLED_ERA5_KF-0_HOM.T. Consistent with the above regarding the lowest simulated MSLP, the ATMOS experiments landfall with a lower MSLP value than the COUPLED ones.

None of the experiments could reproduce the rapid intensification in HO, going from 993 to 923 hPa in 12 h (between 15:00 on October 24 and 03:00 on October 25). Note that the value reported by Hurricane Hunter breaks the trend in MSLP reported in previous PAs.

At this point, these results show that the IC is crucial in simulating the trajectories. In addition, the CP is also important. In ATMOS, using PR option 2 represented a slightly faster system intensification than option 0; however, it increased the distance to the LFP and the landfall time. In COUPLED, the representation of a partially homogenized ocean (HOM.T) improved the result compared to a non-homogenized one regarding landfall time, distance at LFP, and simulated MSLP.

4.1.2 Experiments at a spatial resolution of 10 kilometers

This section shows the results of the experiments where we increased the spatial resolution to 10 km. In ATMOS, the sensitivity analysis involves changes in the CP, RP, DT, and CUDT (when using KF).
For COUPLED experiments, we used KF in all experiments along with DT30. The modifications were made in the IC for the ocean, using different databases (ERA5, OISST 0.25 and OISST 0.50) as the SST field and modifications in the vertical structure of the IC by total or partial homogenizing the upper ocean levels. In addition, we change the RP and CUDT.

4.1.2.1 Atmospheric experiments at a spatial resolution of 10 kilometers

Figure 5 shows the results from the ATMOS experiments. Experiments with the ERA5_KF configuration simulated the trajectory of HO toward the coast. In this configuration, DT30 experiments simulated landfall with a minor time difference compared to their DT60 counterparts, as seen in KF-0_DT60_CUDT5 (+5H) compared to KF-0_DT30_CUDT5 (+4H) and KF-2_DT60_CUDT5 (+6H) compared to KF-2_DT30_CUDT5 (+4H).

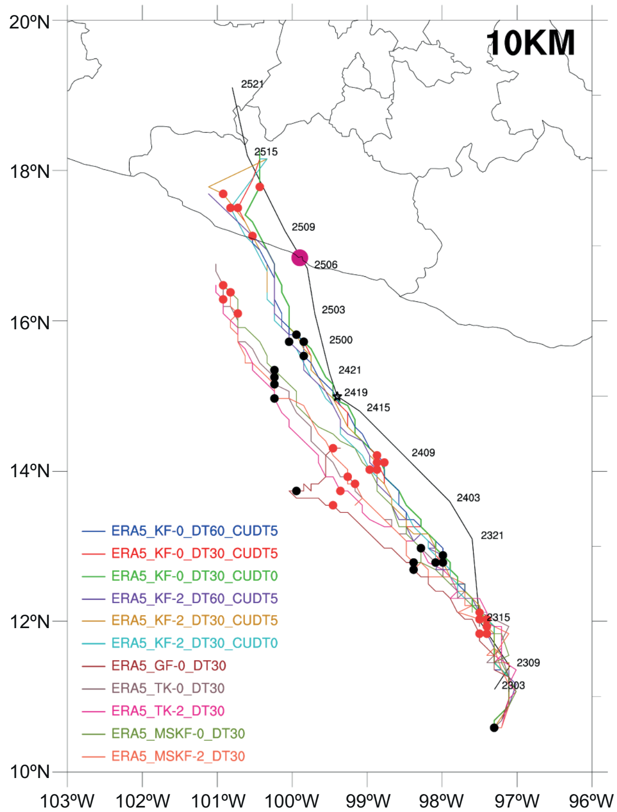

Fig. 5. Simulated trajectories of Hurricane Otis in ATMOS 10KM experiments. Lines of different colors represent trajectories. The black line corresponds to the trajectory reported by NHC. Simulated trajectories start at 00:00 on October 23, while the reported trajectory starts at 03:00.

Concerning the increase in CUDT, in the KF-0_DT30 experiments, the time and distance difference to the LFP were reduced, going from +4H and 74.42 km in KF-0_DT30_CUDT5 to +2H and 47.73 km in KF-0_DT30_CUDT0 (this being the best result in the ATMOS set); on the contrary, when we increased CUDT in KF-2_DT30, the arrival time remains without change, but the LFP distance increased from 74.42 to 83.91 km.

The modifications in the CP did not yield favorable results. When using GF, the trajectory exhibits the same behavior as its counterpart at 15 km spatial resolution, remaining over the ocean until the end of the analysis. In the experiments where we used

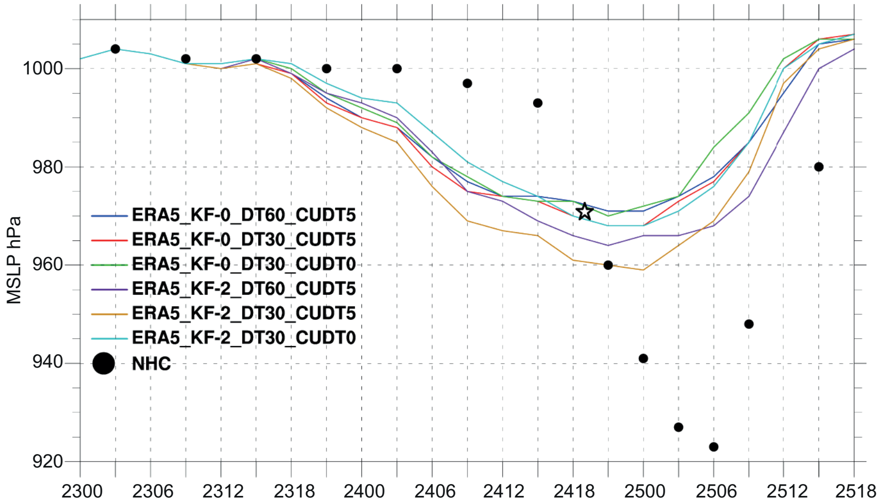

Fig. 6. Simulated MSLP of the ATMOS 10KM experiments that made landfall. The colors associated with each experiment are consistent with Figure 5. Black dots represent NHC data.

TK and MSKF, the trajectories show a movement towards land but tend to deviate from the reported trajectory; at the end of the analysis, the system remains far from the coast.

In general, we observe that when using RP option 0, the simulated trajectories stay closer to the reported trajectory, while using option 2, they move away. This behavior is consistent across all CPs.

Figure 6 shows the simulated MSLP that made landfall in the experiments. Overall, the MSLP values from the 10KM experiments are lower than the 15KM experiments, i.e. the simulated intensification was higher using 10 km spatial resolution than 15 km. In general, we observe that the minimum MSLP in KF-2 is lower than in the respective KF-0 experiments; among these, the DT30_CUDT5 experiments were more intense than the DT60_CUDT5, while the DT30_CU0 simulated the highest MSLP of all. The minimum MSLP value was simulated in KF-2_DT30_CUDT5, reaching 959.1 hPa, which is also the experiment that made landfall with the lowest MSLP value of 984.94 hPa.

4.1.2.2 Coupled experiments at a spatial resolution of 10 kilometers

Figure 7 shows the trajectories of COUPLED experiments using 10 km spatial resolution. We used KF as the CP in the whole set, and all HO simulated

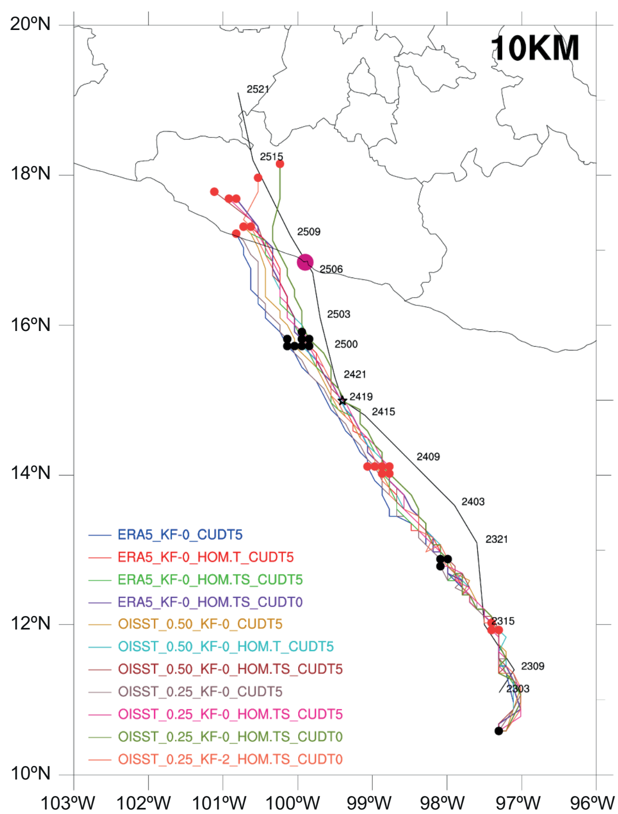

Fig. 7. Simulated trajectories of Hurricane Otis in COUPLED 10KM experiments. Lines of different colors represent trajectories. The black line corresponds to the trajectory reported by NHC. Simulated trajectories start at 00:00 on October 23, while the reported trajectory starts at 03:00.

trajectories made landfall. They follow a similar displacement pattern, but landfalling in different coastal locations.

We observe that experiments with a homogenized ocean, regardless of the SST used as the surface field in the IC, simulated a better approximation in both the impact time and distance to the LFP than a non-homogenized ocean. In congruence with this, the three KF-0_HOM.TS_CUDT5 experiments simulated landfall at 09:00 (+3H), with ERA5_KF-0_HOM.TS_CUDT5 being the best approximation, differing only 57.88 km from the LFP. Conversely, experiments without homogenization (KF-0_CUDT5) show greater arrival time and distance differences. In general, trajectories do not show significant sensitivity to using different SSTs to create the IC in the ocean, which is more evident in the KF-0_HOM.TS_CUDT5 experiments.

Regarding the increase in the frequency of calls to the CP scheme (CUDT0) applied to the HOM.TS experiments, the two experiments with this configuration represent the best approximations of the actual trajectory of HO in all experiments: ERA5_KF-0_HOM.TS_CUDT0 simulates landfall at a distance of 46.38 km, while OISST_0.25_KF-0_HOM.TS_CUDT0 makes landfall at 37.71 km, both at 08:00 (+2H).

In the simulated MSLP (Fig. 8), most experiments simulated MSLP values lower than 967 hPa using the KF-0 configuration, with the lowest value observed in ERA5_KF-0_HOM.TS_CUDT5 at 959.21 hPa. These lower values resulting from the simplified coupling ocean-atmosphere influenced the majority of experiments making landfall with lower MSLP values than the ATMOS_ensemble; ERA5_KF-0_HOM.TS_CUDT0 made landfall with a value of 983.02 hPa.

Experiments with homogenized upper-level oceans (HOM.TS) show higher maximum intensity (lower MSLP) at the time of landfall than those without homogenization. Notice that, in contrast with ATMOS, by increasing CUDT in the COUPLED simulations, the KF-0_HOM.TS_CUDT0 experiments simulated a slightly lower maximum intensity (approximately 1.5 hPa lower) than the KF-0_HOM.TS_CUDT5 experiments.

4.1.3 Experiments at a spatial resolution of 5 kilometers

Figure 9 shows the trajectories. We see that both KF-0 experiments simulated the trajectory toward the coast, showing the same behavior as its counterpart at 10 and 15 km spatial resolutions but showing a better approximation to the reported trajectory for most of the simulation. In this set of experiments,

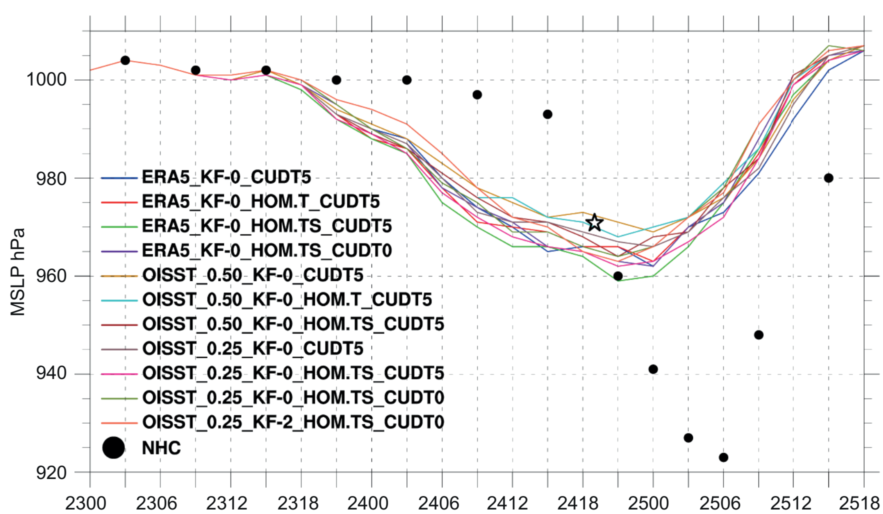

Fig. 8. Simulated MSLP of the COUPLED 10KM experiments that made landfall. The colors associated with each experiment are consistent with Figure 7. Black dots represent NHC data.

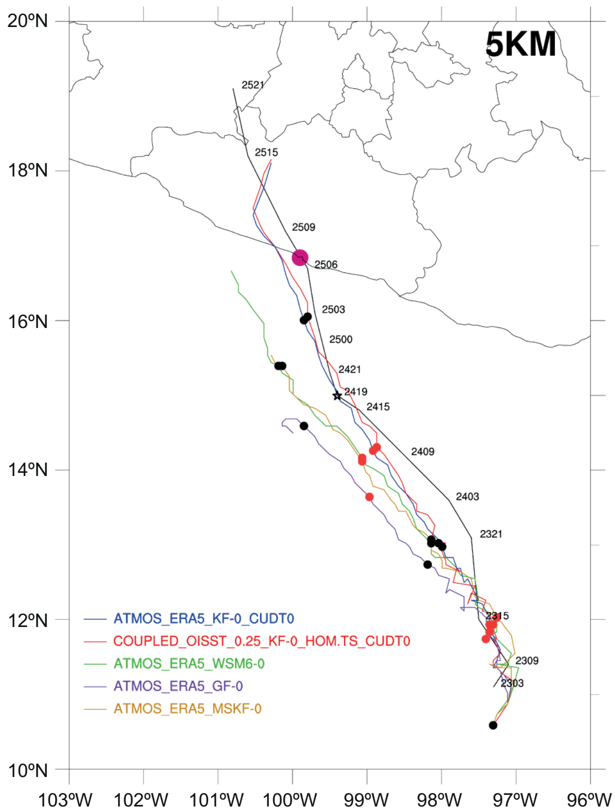

Fig. 9. Simulated trajectories of Hurricane Otis in 5KM experiments. Lines of different colors represent trajectories. The black line corresponds to the trajectory reported by NHC. Simulated trajectories start at 00:00 on October 23, while the reported trajectory starts at 03:00.

COUPLED was slightly better. Both experiments simulate landfall at 39.59 km from the LFP, with landfall time in ATMOS at 06:00 (+0H) and 0500 (–1H) in COUPLED.

The simulated trajectories in the MSKF-0 and WSM6-0 experiments exhibit similar behavior toward land but tend to deviate from the reported trajectory; at the end of the analysis, both are still over the ocean. Finally, the GF-0 experiment, during the first approximately 48 h, simulated a northwestward trajectory, later showing a curvature towards the southeast. Until the end of the simulation, the simulated system remains over the ocean.

Figure 10 shows the MSLP from KF-0 experiments. Both experiments show consistent values during the first 33 h, with ATMOS slightly intensifying. The ATMOS experiment simulated a minimum MSLP value of 960.73 hPa. It made landfall with a value of 983.29 hPa, while the COUPLED experiment simulated a minimum of 961.9 hPa and made landfall with a value of 983.79 hPa. Both experiments simulated lower MSLP values than experiments with the same configuration but at 10 km resolution. These differences are more pronounced in ATMOS than in COUPLED. In ATMOS, we observed variations of up to 10 hPa in the simulation of minimum MSLP and 5 hPa in the landfall MSLP. In COUPLED, the differences in minimum MSLP and landfall MSLP are about two hPa.

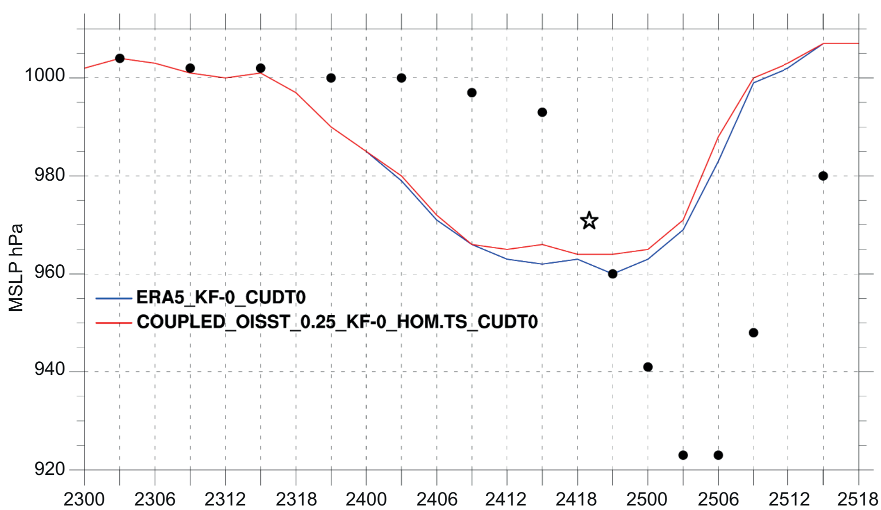

Fig. 10. Simulated MSLP of the 5KM experiments that made landfall. The colors associated with each experiment are consistent with Figure 9. Black dots represent NHC data.

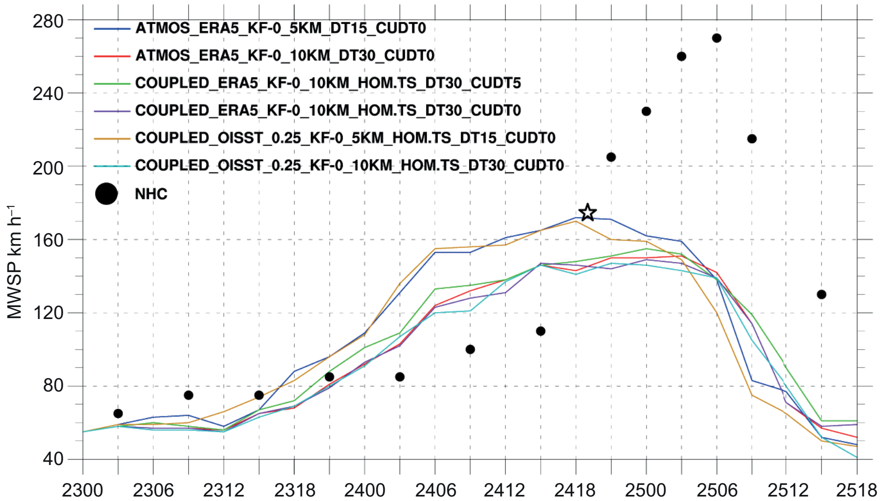

Fig. 11. MWSP simulated in the considered best experiments. MWSP are represented by lines of different colors. Black dots represent NHC data.

Table SI in the supplementary material presents a detailed summary of all ATMOS experiments, and Table SII of COUPLED experiments, showing the MSLP values and the forecast hour at which they occurred. Additionally, for experiments that made landfall, the MSLP value at the time of landfall is reported, along with the time elapsed from the start of the forecast and its corresponding landfall time in UTC. We also compare the time and distance differences to the NHC reports.

4.2 Maximum wind speed at 10 meters

Figure 11 shows the MWSP associated with HO from the experiments with the best performance. Generally, we observe a gradual increase in speeds, reaching maximums of approximately 150-160 km h^{-1} in 10KM experiments and 170 km h^{-1} in 5KM experiments. All values between 03:00 and 15:00 on October 24 are higher than those reported in the PA. After their respective peaks, a speed decrease is evident, attributed, among other factors, to the hurricane's interaction with the landmass (Chan et al., 2001) and the abrupt loss of energy extracted from the ocean through latent heat (Wong et al., 2008).

In the reported values for HO, there is an abrupt increase in speed between the reported values in the Hurricane Hunter aircraft flight (star marker) and the previous point. The reported HO wind speed at landfall was 270 km h^{-1}, around 100 km h^{-1} higher than the maximum simulated wind speeds.

Figure 12 corresponds to the simulated wind fields at 10 m (vectors and color contours) and MSLP (contour lines), giving a horizontal view of the HO structure. Each column in this figure represents an experiment titled at the top of the column: ATMOS_ERA5_KF-0_5KM_CUDT0, ATMOS_ERA5_KF-0_10KM_DT30_CUDT0, COUPLED_OISST_0.25_KF-0_5KM_HOM.TS_CUDT0 and COUPLED_OISST_0.25_KF-0_10KM_HOM.TS_DT30_CUDT0. The upper row corresponds to the time (indicated in each image) when the experiment simulates the landfall. In the following rows (from top to bottom), the images correspond to –2 h concerning the upper image and go up to –10 h. As observed in the trajectories (see Figs. 7 and 9), the positions in the hours preceding landfall are similar in the four experiments.

The HO's eye structure and the bands around it are consistent between experiments with identical spatial resolution. Generally, in experiments at a spatial resolution of 5 km, a more compact structure of the HO is observed regarding the system's center, while the structure is broader at a spatial resolution of 10 km. We observe well-defined circles in the images at –10H and –8H with MWSP between 120 and 155 km h^{-1} in all experiments and some areas with values between 155 and 180 km h^{-1} in 5KM experiments.

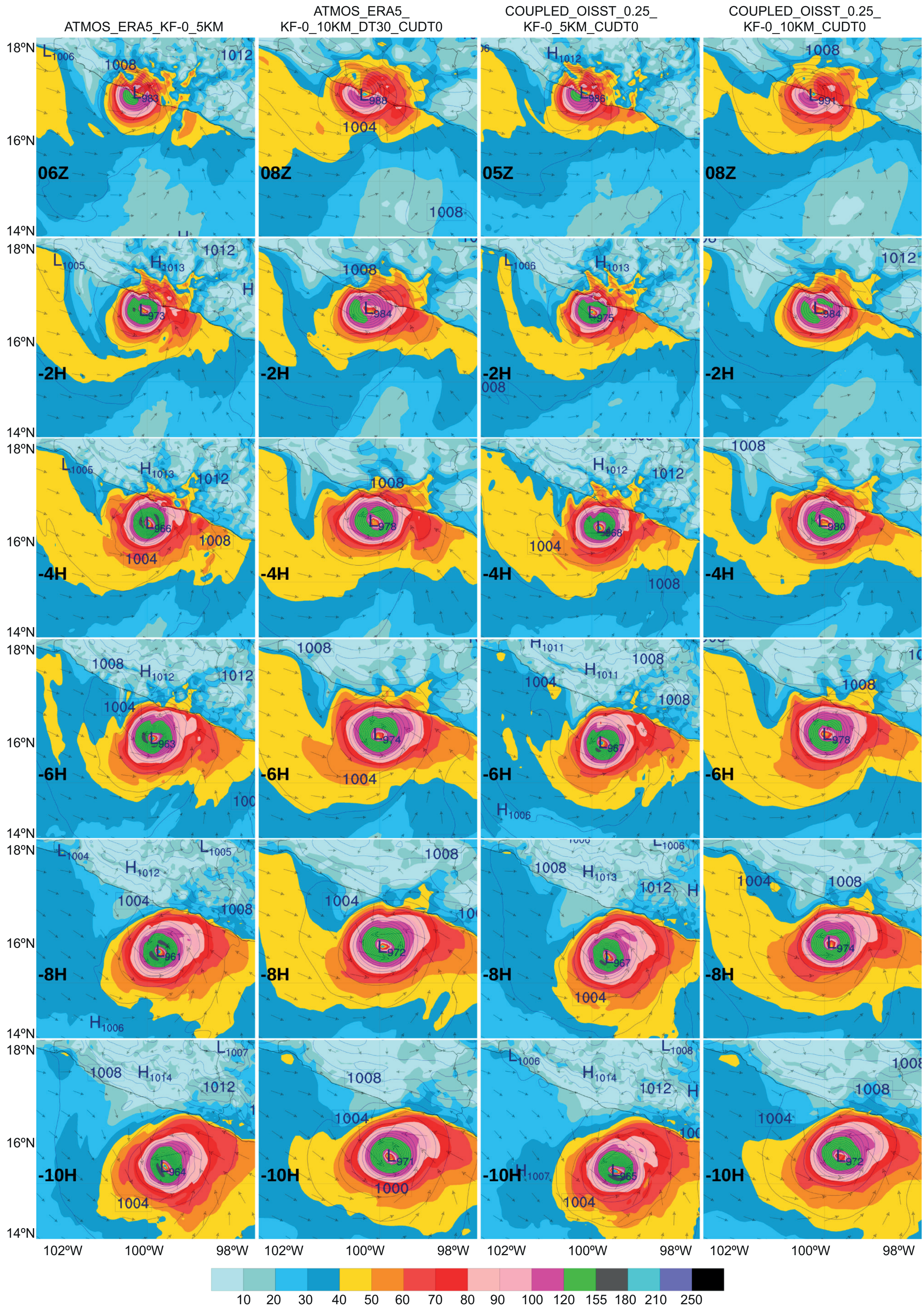

Fig. 12. Wind speed at 10 m (vectors and color contours) and simulated MSLP (contour lines). Column 1: ATMOS_ERA5_KF-0_5KM_CUDT0. Column 2: ATMOS_ERA5_KF-0_10KM_DT30_CUDT0. Column 3: COUPLED_OISST_0.25_KF-0_5KM_HOM.TS_CUDT0. Column 4: COUPLED_OISST_0.25_KF-0_10KM_HOM.TS_CUDT0.

For the 10KM experiments, from –6H they show interaction with the coastal area, causing the circles of maximum speeds to begin deforming; in ATMOS, the interaction is slightly less, so the structure is still better defined. In the subsequent hours, the interaction with the coastal areas diminishes the regions with maximum speeds around the eye in both experiments. Only the COUPLED experiment exhibits areas near the coast with speeds exceeding 120 km h^{-1} 2 h before landfall. Both experiments show a MWSP value of about 120 km h^{-1} at landfall.

In experiments at a spatial resolution of 5 km, circles with MWSP values of 155 km h^{-1} remain well-structured from –10H to –2H before landfall. During this time, in ATMOS, broader areas with speeds between 155 and 180 km h^{-1} are observed, while in COUPLED, these are smaller. At landfall, both experiments predominantly display maximum values of 120 km h^{-1} but also present a secondary area with maximum winds of 155 km h^{-1}.

At landfall time, the simulated systems with a spatial resolution of 5 km maintain a more coherent circular structure, as indicated by their greater isobars density than those observed in experiments at 10 km.

4.3 Analysis of the initial condition

To analyze the differences between the initial atmospheric vertical structure represented in GFS and ERA5 that could have influenced HO's development, we obtained a zonal cross-section for variables P (pressure perturbation) and V (y-wind component) and a meridional cross-section for variables P and U (x-wind component). Figure 13 shows the cross-sections. The first column corresponds to the IC from GFS, and the second represents the IC from ERA5. Each panel indicates the respective variable. The blue box in each image highlights the position of HO.

In ERA5's zonal P (Fig. 13b), within the blue box, there is an area with negative values extending from 800 to 100 hPa and low P values near the surface. Consequently, significant pressure gradients exist at the lower and middle levels of the atmosphere, which can be directly associated with the vertical structure observed in zonal V (Fig. 13d). Here, we observe a well-defined wind system, clearly symmetric around the system's center, from the surface to higher atmospheric levels. This meridional wind field indicates a low vertical shear, favoring conditions for HO's development.

In GFS (Fig. 13a), we observe negative P values from 600 hPa to the top of the atmosphere but with lower magnitudes; as a result, the pressure gradients are weaker, implying weaker meridional winds. Figure 13c shows the zonal cross-section of the V field of GFS. The meridional wind system vertical structure associated with HO is present from the surface up to approximately 550 hPa but with lower magnitude values than those from ERA5. Note that between 550 and 450 hPa, mainly negative values are present, limiting the coherent vertical structure of the meridional wind system. Thus, the pattern observed in the meridional wind field indicates the presence of strong vertical wind shear in the meridional wind values of GFS used as IC.

Meridionally, the P field shows a similar behavior to the one described zonally: GFS (Fig. 13e) with a weak pressure gradient compared to those observed in ERA5 (Fig. 13f). In the meridional U field from ERA5 (Fig. 13h), we observe the clearly defined and symmetric structure of the zonal winds associated with HO, from the surface up to higher atmospheric levels; in contrast, in the meridional U field from GFS (Fig. 13g), the vertical system's structure is observed only up to about 600 hPa, clearly restricted by positive wind values northward of the center of the initial perturbation at the middle and high atmospheric levels. Therefore, similar to the zonal-cross sections, the vertical distributions of the corresponding wind fields indicate lower vertical gradients in ERA5 but higher vertical gradients in GFS, favoring conditions for storm development in ERA5 and hindering conditions in GFS.

4.4 Analysis of the temporal evolution of environmental factors using GFS and ERA5

Previous studies have shown the importance of the interaction between TC circulations and large-scale environmental fields, as well as with the ocean (Wang, 2002a, b; Wang and Wu, 2004).

For instance, it is known that SST is crucial for providing energy to TCs, influencing their development and intensification (Gao et al., 2016). Further inspection of Figure 2a, b suggests that SST was not a determining factor in the GFS-based forecast failure, as comparable magnitudes with those of ERA5 are generally observed in the area of the initial perturbation (see also Fig. S6 in the supplementary material).

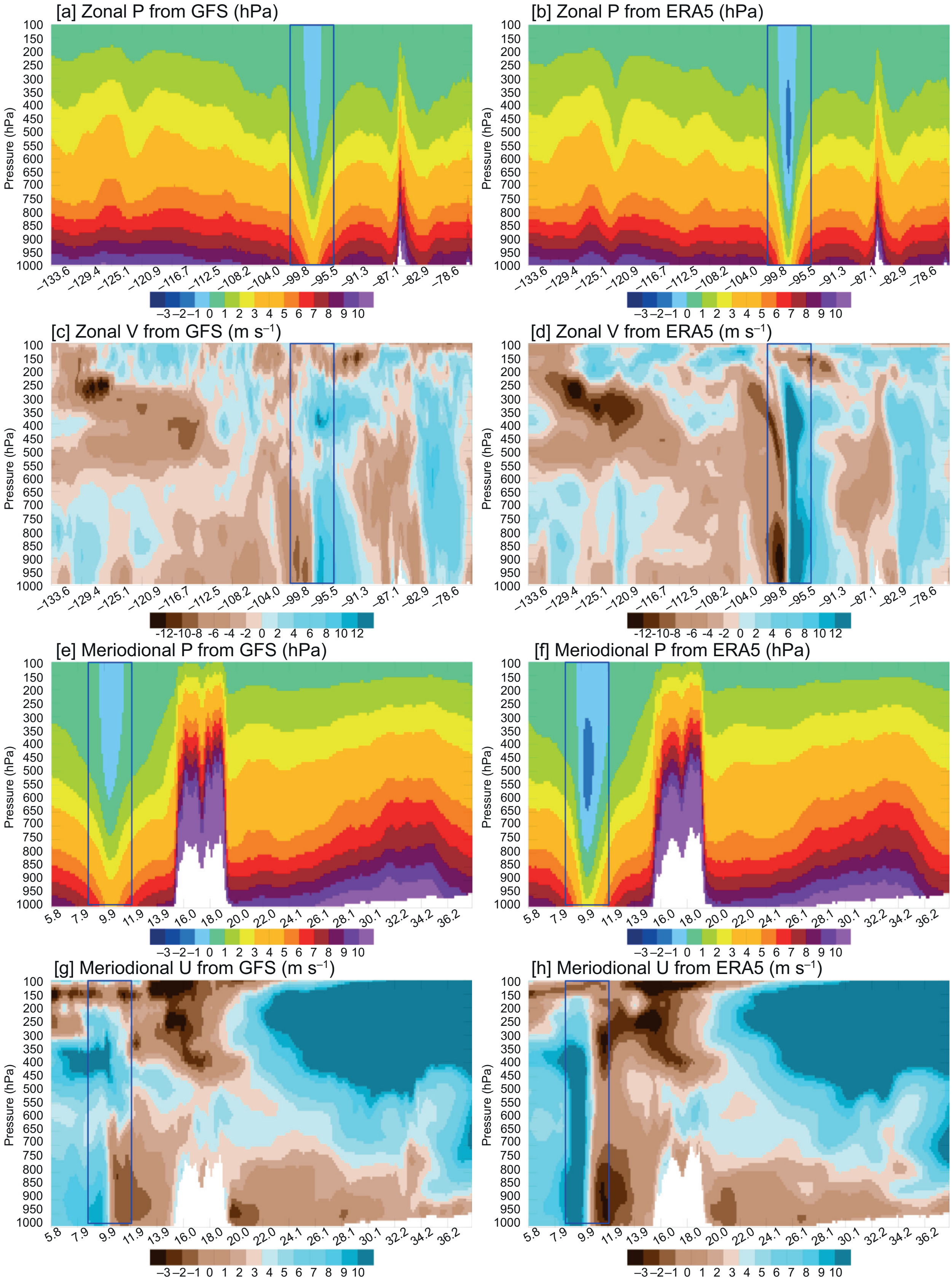

Fig. 13. Cross-section of the initial conditions for P, U, and V, of GFS and ERA5. (a) Zonal cross-section of P from GFS. (b) Zonal cross-section of P from ERA5. (c) Zonal cross-section of V from GFS. (d) Zonal cross-section of V from ERA5. (e) Meridional cross-section of P from GFS. (f) Meridional cross-section of P from ERA5. (g) Meridional cross-section of U from GFS. (h) Meridional cross-section of V from ERA5. The blue box in each image highlights the position of HO.

Regarding environmental factors, according to various authors (e.g., Chan and Gray, 1982; Chan et al., 2002), the ESF is one of the most critical factors in determining TC displacement. An ESF misrepresentation, mainly due to weak flow, can lead to considerable track errors in the forecast (Torn et al., 2018; Miller and Zhang, 2019; Ashcroft et al., 2021). A rapid intensification of a TC occurs when favorable environmental conditions are present, such as weak vertical wind shear (VWS), high mid-lower tropospheric RH, and high CAPE (Kaplan and DeMaria, 2003; Hendricks et al., 2010; Kaplan et al., 2010; Shu et al., 2012; Wang et al., 2015). Figure 14a shows the ESF of the ATMOS_GFS_KF-0_15KM experiment, calculated at each layer between 850 and 250 hPa. Black arrows indicate the average simulated wind values (before storm removal) within the same ESF radius, while blue arrows represent the ESF. Arrows orientation and length indicate the direction and magnitude, respectively. The *x*-axis represents simulation time. Overall, the simulated average wind is comparable to the ESF. During the first 18 h, a weak ESF is observed between 850 and 500 hPa, with wind direction varying with pressure. At 450 hPa, there is an increase in wind speed, with an eastward direction opposite to the direction at 850 hPa, indicating strong VWS between 450 hPa and lower levels. As the hours pass, an increase in magnitude is observed at 850 hPa and a decrease in upper levels above 500 hPa. This suggests that the simulated system begins to develop and increase its thickness in the atmospheric column (see Figs. S1 and S2 in the supplementary material). Despite this, the wind direction maintains its changing behavior vertically. After hour 30, the ESF vectors are primarily oriented towards the northwest between 750 and 450 hPa, consistent with the main reported direction of the HO. However, starting from hour 48, a clear dominant direction towards the west and southwest is observed in later hours. This behavior responds to the influence of a system associated with Tropical Depression 21 (TD21), which moved at mid-levels toward the west from the Caribbean Sea (in reality, it dissipated over Nicaragua on October 24). This system can be observed in Figure 13c, positioned at approximately 80 ºW, and its unreal intensification and displacement are shown in Figure S2. In the IC (see Figure S3), even the system associated with

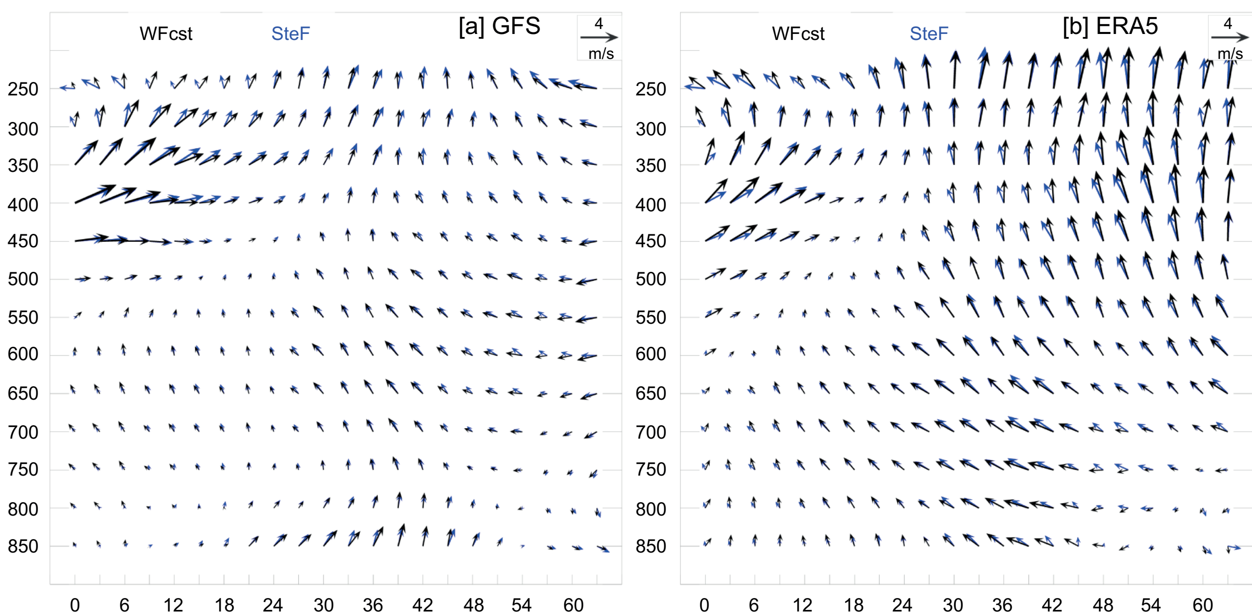

Fig. 14. Wind values calculated at each layer between 850 and 250 hPa within a 3º radius around the simulated storm center. Black arrows represent the average wind values (before storm removal), and blue arrows represent the environmental steering flow. Arrows orientation and length indicate the direction and magnitude, respectively. The *x*-axis represents simulation time. (a) ATMOS_GFS_KF-0_15KM experiment. (b) ATMOS_ERA5_KF-0_15KM.

TD21 shows more significant development and magnitude than that of the HO. Figure S3 shows how the unreal representation of system TD21 affects the ESF of the HO and starts to interact with the simulated HO system. In the continuation of the analysis (not shown) up to hour 84 of simulation, it is observed that both systems enter into a Fujiwhara-type interaction.

On the other hand, Figure 14b shows the results of ATMOS_ERA5_KF-0_15KM. In general, the direction of the ESF has been consistent at all levels since the beginning of the simulation, indicating a weak VWS in response to a better-developed system throughout the column. As the hours pass, the magnitude of the ESF tends to increase at most levels while maintaining consistency in direction. Contrary to GFS, in the IC from ERA5, TD21 is represented with a lower magnitude than HO (Fig. 13d). Despite TD21 showing a westward displacement, it was smaller than GFS's (see Fig. S4). However, the simulated HO translates toward the coast, implying no interaction with TD21, as observed in reality (see Figs. S2 and S4).

Regarding other environmental factors, both the KE (Fig. 15a) and RV (Fig. 15c) simulated in ATMOS_GFS_KF-0_15KM are generally lower than those using ERA5 (Fig. 15b, d, respectively). In GFS, during the initial hours, weak winds and their associated lower KE and RV values and upper-level winds make the perturbation development difficult despite the larger values of CAPE and RH. This suggests that GFS presented a more significant potential for developing a system of greater intensity than ERA5 concerning these variables. However, both the wind shear and the wind magnitude are crucial in controlling the HO initial development.

5. Discussion and conclusions

In this study, we analyze the case of Hurricane Otis (HO), which occurred in the eastern region of the Pacific Ocean from October 22 to 25, 2023), rapidly and unexpectedly making landfall near Acapulco City as a category five hurricane. According to the NHC, HO was the strongest hurricane to land in the eastern Pacific and the first hurricane category five to hit the Mexican Pacific coasts. The reported intensity far exceeded the estimates derived from satellite image analysis. In the previous days, the operational available national weather forecast (NWF), including official and unofficial NWFs, failed to predict HO trajectory and intensification.

TThe main aim of this study is to analyze the reasons for the failure of both official and unofficial NWFs issued by SMN and ICAyCC, respectively. We used GFS as the IC, which we knew a priori gave poor results. Afterward, we replicate the experiment using information from ERA5 for the IC. Our aim in using ERA5 is to analyze its better atmospheric representation and how it can help us understand the deficiencies of GFS in representing the initial atmospheric structure that led to forecast failure. In pursuing the mentioned objective, we conducted two experiments (ATMOS_GFS_KF-0_15KM and ATMOS_ERA5_KF-0_15KM) using only the coupled system's atmospheric component (WRF).

Our results show that although some variables in the GFS data, such as RH, CAPE, and even SST, were more favorable for the development and intensification of the disturbance compared to ERA5, the three-dimensional structure of the wind field in the eastern tropical Pacific did not contribute to the initial development of HO. A weak ESF at levels below 500 hPa, corresponding large vertical gradients, and a strong shear at 450 hPa, significantly inhibited the vertical development of the disturbance associated with the HO, constraining its development to lower and middle atmospheric levels. Thus, in the early hours of the system's evolution, it is weak with an erratic trajectory. When the system's structure begins to organize and move northwestward, an unreal interaction with a low-pressure system that moved westward from the Caribbean Sea (associated with TD21) modifies the simulated HO direction, preventing its approach to the coast.

The GFS model's inability to accurately represent the wind's state in the atmosphere has direct implications for the accuracy of tropical cyclone simulations. This limitation is particularly evident in the eastern tropical Pacific, a critical region where tropical storms originate and later develop into cyclones. The need for observational data in this region is therefore paramount.

As anticipated, the ATMOS_ERA5_KF-0_15KM model yielded more promising results. It simulated a trajectory that made landfall at 64.84 km from the LFP with a lead time of +6H. However, it is worth

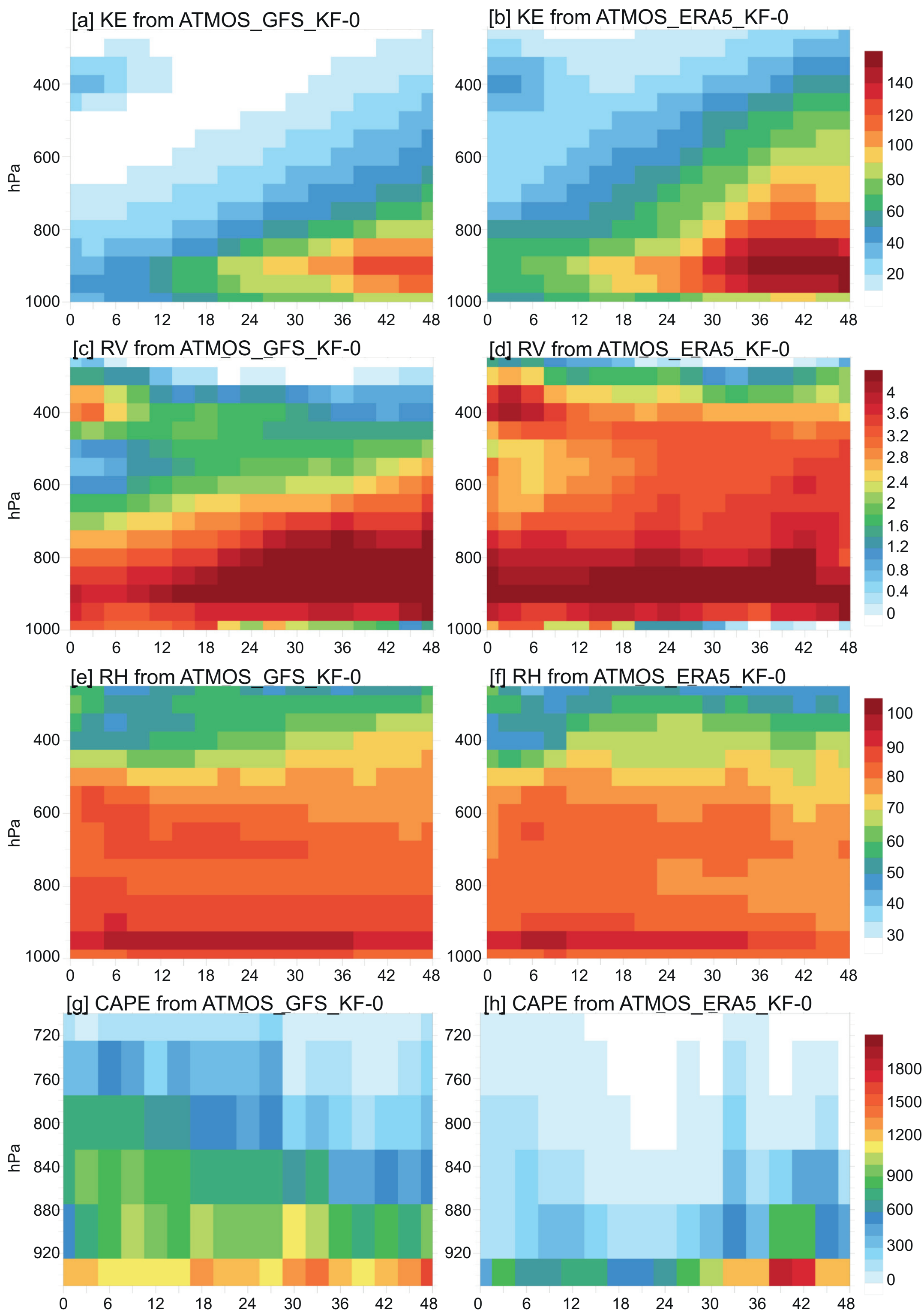

Fig. 15. Average values of environmental factors within the same ESF radius in each layer. The values represent the magnitude at each pressure level; they do not represent the value at the layer thickness. (a-b) Kinetic energy. (c-d) Relative vorticity. (e-f) Relative Humidity. (g-h) CAPE. The first column corresponds to the GFS experiment, and the second corresponds to the ERA5 experiment.

noting that despite these improvements, the model still struggles to capture maximum intensity and rapid intensification. This suggests that further refinement is needed to fully exploit the potential of this model in improving TC simulations.

Additionally, to analyze the model's sensitivity in simulating the trajectory and intensity of the HO, we conducted numerical experiments involving modifications in IC for the atmosphere and the ocean, spatial resolution, roughness parameterization, CP schemes, and different time steps for the temporal integration and calls to the CP scheme (only with KF). For this purpose, we employed the coupled system WRF-PWP.

Various studies in the literature have shown that the trajectory of a hurricane is highly sensitive to the choice of CP scheme (Parker et al., 2017; Shepherd and Walsh, 2017; Zhang et al., 2017; Saunders et al., 2019). Consequently, we conducted ATMOS experiments using four different CP schemes to analyze the model's sensitivity in simulating the HO trajectory. Our results indicate that KF performed best in simulating the trajectory, findings consistent with those observed by Marras et al. (2017) and Saunders et al. (2019). The remaining schemes yielded unacceptable results, with GF showing the poorest performance. Additionally, we examined how different CP schemes responded to changes in the model's spatial resolution, conducting a series of ATMOS experiments with spatial resolutions of 10 and 5 km. The results did not generally show significant changes; only using the KF scheme with increased spatial resolution led to improved trajectory and simulated MSLP outcomes. Notice that the 5 km resolution falls within the so-called grey zone (Hong and Dudhia, 2012), where we need to elucidate whether a CP scheme is necessary or must resolve deep convection explicitly. Some authors have used scale-aware CP to address this issue in recent years (e.g., Kwon and Hong, 2016; Mahoney, 2016; Park et al., 2022). Therefore, we also analyzed the model's performance using scale-aware GF and MSKF schemes. In these cases, both schemes yield unsatisfactory results.

Within KF, we can adjust the time step to call the cumulus routines (cudt). We tried calling at every model time step (CUDT0) and every 5 min (CUDT5). Overall, we get better results in the CUDT0 experiments.

Regarding roughness, in all experiments where we used RP option 2, lower MSLP values were simulated compared to the RP option 0 (consistent with Green and Zhang [2017] and Greeshma et al. [2019]). However, RP option 2 increased the distance to the LFP, consistent with the findings of Greeshma et al. (2019).

ATMOS-KF experiments show that increased spatial resolution improved outcomes in the simulated trajectory. For the best results in 15KM, 10KM, and 5KM, the corresponding values for the distance to LFP are 64.84, 47.73, and 39.59 km; the landfall MSLP are 989.85, 988.45, and 983.29 hPa; and the landfall-time are +6H, +2H, and +0H. However, increasing spatial resolution significantly increases the computational time required for the simulation (approximately 30 min using a spatial resolution of 15 km, 1:15 h using 10 km, and 9 h using 5 km).

After establishing the significance of the CP scheme and the effects of spatial resolution, the last point of our study is to analyze the importance of incorporating the effect of an active ocean in the HO simulation. For this purpose, we conducted a series of COUPLED experiments using the WRF-PWP system. We examined the sensitivity of the WRF-PWP system to different SST fields prescribed as IC for the simplified ocean. Additionally, we studied changes in the vertical structure of the upper ocean layers by increasing the mixing layer's depth. The results indicate that homogenization of the upper ocean thermal structure improved the trajectory and intensity of HO, which is consistent with the findings of Miyamoto et al. (2017) and Fudeyasu et al. (2018). A homogeneous density layer with a high energy content emerges in the experiments with homogenization of both temperature and salinity. Consequently, more energy is available for the simulated system than in the experiments without homogenization, enhancing the trajectory, intensity, and arrival time. For instance, in the non-homogenized ERA5-10KM_CUDT5 experiment, we observed a landfall MSLP of 992.49 hPa, with an arrival time of +6H at a distance of 107.08 km from the LFP.

In contrast, the fully homogenized ERA5_10KM_HOM.TS_CUDT5 shows a landfall MSLP of 986.36 hPa, an arrival time of +3H, and a distance of 57.88 km from the LFP. The partially homogenized

HOM.T results lie in between these values. The results do not exhibit significant sensitivity to different initial SST fields. Consistent with ATMOS, we obtained the best outcomes using CUDT0, with significant improvement as the resolution increased.

The best results from the two sets of experiments at 10 km were obtained in ATMOS_ERA5_KF-0_10KM_DT30_CUDT0, which simulated a minimum MSLP of 970.91 hPa, a landfall MSLP of 988.45 hPa, and a landfall time of +2H at a distance of 47.73 km from the LFP. On the other hand, COUPLED_OISST_0.25_KF-0_HOM.TS_CUDT0 yielded a minimum MSLP of 963.98 hPa, a landfall MSLP of 986.06 hPa, and a landfall time of +2H at 37.71 km from the LFP. At a 5 km resolution, ATMOS_ERA5_KF-0_5KM_CUDT0 simulated a minimum MSLP of 960.73 hPa, a landfall MSLP of 983.29 hPa, and a landfall time of +0H, while COUPLED_OISST_0.25_KF-0_HOM.TS_CUDT0 simulated a minimum MSLP of 961.9 hPa, a landfall MSLP of 983.79 hPa, and a landfall time of –1H. Both experiments were at a distance of 39.59 km from the LFP. Our results indicate that COUPLED outperformed ATMOS at 10 km resolution across various analyses. However, at 5 km resolution, both model configurations displayed very similar results; the primary distinction was the arrival time, where COUPLED simulated landfall 1 h earlier than ATMOS.

These model sensitivity tests represent a first approach to determining an appropriate setup for simulating TCs in the eastern tropical Pacific. A second stage of the research will address a more in-depth analysis of these experiments, including more case studies and other data for the IC. Notice that the reported MSLP by NHC indicates a sustained decrease in the low pressure associated with HO. Contrary to our simulations, there is no sign of a weakening as the hurricane interacts with the coast. We consider that such evolution, without a sign of weakening, is physically impossible. This topic, however, goes beyond the objectives of this work.

We need to address numerous remaining questions about HO. An in-depth analysis of the environmental factors that contributed to its rapid intensification is crucial to understanding its associated processes and how we can adequately represent them in NWP models. For example, reanalysis data show the existence of substantial cyclonic vorticity inputs at 850 hPa associated with the Tehuanos wind, which could have influenced the intensification of the HO.

Acknowledgments

CONAHCyT supported the research through a doctoral scholarship from the first author. The Secretaría de Ciencia y Tecnología e Innovación de la Ciudad de México (SECITI/050/2016; SECITI/057/2017) partially funded the computational resources.

References

Aquino-Martínez LP, Ortega-Guerrero B, Quintanar AI, Ochoa-Moya CA, Barrón-Fernández R. 2023. High-performance computing with the Weather Research and Forecasting System model: A case study under stable conditions over Mexico basin. Computación y Sistemas 27: 627-641. https://doi.org/10.13053/cys-27-3-4035

Arakawa A. 2004. The cumulus parameterization problem: Past, present, and future. Journal of Climate 17: 2493-2525. https://doi.org/10.1175/1520-0442(2004)017<2493:RATCPP>2.0.CO;2

Ashcroft J, Schwendike J, Griffiths SD, Ross AN, Short CJ. 2021. The impact of weak environmental steering flow on tropical cyclone track predictability. Quarterly Journal of the Royal Meteorological Society 147: 4122-4142. https://doi.org/10.1002/qj.4171

Banzon V, Smith TM, Chin TM, Liu C, Hankins W. 2016. A long-term record of blended satellite and in situ sea-surface temperature for climate monitoring, modeling and environmental studies. Earth System Science Data 8: 165-176. https://doi.org/10.5194/essd-8-165-2016

Beljaars ACM. 1995. The parametrization of surface fluxes in large-scale models under free convection. Quarterly Journal of the Royal Meteorological Society 121: 255-270. https://doi.org/10.1002/qj.49712152203

Biswas MK, Bernardet L, Dudhia J. 2014. Sensitivity of hurricane forecasts to cumulus parameterizations in the HWRF model. Geophysical Research Letters 41: 9113-9119. https://doi.org/10.1002/2014GL062071

Brutsaert W. 1975. A theory for local evaporation (or heat transfer) from rough and smooth surfaces at ground level. Water Resources Research 11: 543-550. https://doi.org/10.1029/WR011i004p00543

Bruyère CL, Holland GJ, Towler E. 2012. Investigating the use of a genesis potential index for tropical cyclones in the North Atlantic basin. Journal of Climate 25: 8611-8626. https://doi.org/10.1175/JCLI-D-11-00619.1

C3S. 2021. ORAS5 global ocean reanalysis monthly data from 1958 to present. Copernicus Climate Change Service, Climate Data Store. https://doi.org/10.24381/cds.67e8eeb7 (accessed November 2023)

Chan JCL, Gray WM. 1982. Tropical cyclone movement and surrounding flow relationships. Monthly Weather Review 110: 1354-1374. https://doi.org/10.1175/1520-0493(1982)110%3C1354:TCMASF%3E2.0.CO;2

Chan JCL, Duan Y, Shay LK. 2001. Tropical cyclone intensity change from a simple ocean-atmosphere coupled model. *Journal of the Atmospheric Sciences 58*: 154-172. https://doi.org/10.1175/1520-0469(2001)058<0154:TCICFA>2.0.CO;2

Chan JCL, Ko FMF, Lei YM. 2002. Relationship between potential vorticity tendency and tropical cyclone motion. Journal Atmospheric Sciences 59: 1317-1336. https://doi.org/10.1175/1520-0469(2002)059<1317:RBPVTA>2.0.CO;2

Chandrasekar R, Balaji C. 2012. Sensitivity of tropical cyclone Jal simulations to physics parameterizations. Journal of Earth System Science 121: 923-946. https://doi.org/10.1007/s12040-012-0212-8

Charnock H. 1955. Wind stress on a water surface. Quarterly Journal of the Royal Meteorological Society 81: 639-640. https://doi.org/10.1002/qj.49708135027

Davis C, Wang W, Dudhia J, Torn R. 2010. Does increased horizontal resolution improve hurricane wind forecasts? Weather and Forecasting 25: 1826-1841. https://doi.org/10.1175/2010WAF2222423.1

Donelan MA, Haus BK, Reul N, Plant WJ, Stiassnie M, Graber HC, Brown OB, Saltzman ES. 2004. On the limiting aerodynamic roughness of the ocean in very strong winds. Geophysical Research Letter 31: L18306. https://doi.org/10.1029/2004GL019460

Dorman CE, Carniel S, Cavaleri L, Sclavo M, Chiggiato J, Doyle J, Haack T, Pullen J, Grbec B, Vilibić I, Janeković I, Lee C, Malačič V, Orlić M, Paschini E, Russo A, Signell RP. 2006. February 2003 marine atmospheric conditions and the bora over the northern Adriatic. Journal of Geophysical Research: Oceans 111: C03S03. https://doi.org/10.1029/2005JC003134

Dudhia J. 1989. Numerical study of convection observed during the Winter Monsoon Experiment using a mesoscale two-dimensional model. Journal of the Atmospheric Sciences 46: 3077-3107. https://doi.org/10.1175/1520-0469(1989)046<3077:NSOCOD>2.0.CO;2

Emanuel KA. 1995. The behavior of a simple hurricane model using a convective scheme based on subcloud-layer entropy equilibrium. Journal of the Atmospheric Sciences 52: 3960-3968. https://doi.org/10.1175/1520-0469(1995)052<3960:TBOASH>2.0.CO;2

Emanuel K. 2003. A similarity hypothesis for air-sea exchange at extreme wind speeds. Journal of the Atmospheric Sciences 60: 1420-1428. https://doi.org/10.1175/1520-0469(2003)060<1420:ASHFAE>2.0.CO;2

Fiorino M, Elsberry RL. 1989. Some aspects of vortex structure related to tropical cyclone motion. Journal of the Atmospheric Sciences 46: 975-990. https://doi.org/10.1175/1520-0469(1989)046<0975:SAOVSR>2.0.CO;2

Fudeyasu H, Ito K, Miyamoto Y. 2018. Characteristics of tropical cyclone rapid intensification over the western North Pacific. Journal of Climate 31: 8917-8930. https://doi.org/10.1175/JCLI-D-17-0653.1

Galarneau JT, Davis CA. 2013. Diagnosing forecast errors in tropical cyclone motion. Monthly Weather Review 141: 405-430. https://doi.org/10.1175/MWR-D-12-00071.1

Gao S, Zhai S, Chiu LS, Xia D. 2016. Satellite air-sea enthalpy flux and intensity change of tropical cyclones over the western North Pacific. Journal of Applied Meteorology and Climatology 55: 425-444. https://doi.org/10.1175/JAMC-D-15-0171.1

Gbode IE, Dudhia J, Ogunjobi KO, Ajayi VO. 2019. Sensitivity of different physics schemes in the WRF model during a West African monsoon regime. Theoretical and Applied Climatology 136: 733-751. https://doi.org/10.1007/s00704-018-2538-x

Glotfelty T, Alapaty K, He J, Hawbecker P, Song X, Zhang G. 2019. The Weather Research and Forecasting model with aerosol-cloud interactions (WRF-ACI): Development, evaluation, and initial application. *Monthly Weather Review 147*: 1491-1511. https://doi.org/10.1175/MWR-D-18-0267.1

Green BW, Zhang F. 2013. Impacts of air-sea flux parameterizations on the intensity and structure of tropical cyclones. *Monthly Weather Review 141*: 2308-2324. https://doi.org/10.1175/MWR-D-12-00274.1

Greeshma M, Srinivas CV, Hari Prasad KBRR, Baskaran R, Venkatraman B. 2019. Sensitivity of tropical cyclone predictions in the coupled atmosphere-ocean model WRF-3DPWP to surface roughness schemes. Meteorological Applications: Science and Technology for Weather and Climate 26: 324-346. https://doi.org/10.1002/met.1765

Grell GA, Freitas SR. 2014. A scale and aerosol-aware stochastic convective parameterization for weather and air quality modeling. Atmospheric Chemistry and Physics 14: 5233-5250. https://doi.org/10.5194/acp-14-5233-2014

Haidvogel DB, Arango H, Budgell WP, Cornuelle BD, Curchitser E, Lorenzo ED, Fennel K, Geyer WR, Hermann AJ, Lanerolle L, Levin J, McWilliams JC, Miller AJ, Moore AM, Powell TM, Shchepetkin AF, Sherwood CR, Signell RP, Warner JC, Wilkin J. 2008. Ocean forecasting in terrain-following coordinates: Formulation and skill assessment of the Regional Ocean Modeling System. Journal of Computational Physics 227: 3595-3624. https://doi.org/10.1016/j.jcp.2007.06.016

Hendricks EA, Peng MS, Fu B, Li T. 2010. Quantifying environmental control on tropical cyclone intensity change. Monthly Weather Review 138: 3243-3271. https://doi.org/10.1175/2010MWR3185.1

Hersbach H, Bell B, Berrisford P, Biavati G, Horányi A, Muñoz-Sabater J, Nicolas J, Peubey C, Radu R, Rozum I, Schepers D, Simmons A, Soci C, Dee D, Thépaut JN. 2023. ERA5 hourly data on pressure levels from 1940 to present. Copernicus Climate Change, Service Climate Data Store. https://doi.org/10.24381/cds.bd0915c6 (accessed 06 November 2023).

Holland GJ. 1983. Tropical cyclone motion: Environmental interaction plus a beta effect. Journal of the Atmospheric Sciences 40: 328-342. https://doi.org/10.1175/1520-0469(1983)040<0328:TCMEIP>2.0.CO;2

Hong SY, Dudhia J. 2012. Next-generation numerical weather prediction: Bridging parameterization, explicit clouds, and large eddies. Bulletin of the American Meteorological Society 93: ES6-ES9. https://doi.org/10.1175/2011bams3224.1

Hong SY, Lim JJO. 2006. The WRF Single-Moment 6-Class Microphysics Scheme (WSM6). Asia-Pacific Journal of Atmospheric Sciences 42: 129-151.

Hong SY, Noh Y, Dudhia J. 2006. A New Vertical diffusion package with an explicit treatment of entrainment processes. Monthly Weather Review 134: 2318-2341. https://doi.org/10.1175/MWR3199.1

Huang B, Liu C, Banzon V, Freeman E, Graham G, Hankins B, Smith T, Zhang HM. 2021. Improvements of the Daily Optimum Interpolation Sea Surface Temperature (DOISST) version 2.1. Journal of Climate 34: 2923-2939. https://doi.org/10.1175/JCLI-D-20-0166.1

Kain JS. 2004. The Kain-Fritsch convective parameterization: An update. Journal of Applied Meteorology and Climatology 43: 170-181. https://doi.org/10.1175/1520-0450(2004)043<0170:TKCPAU>2.0.CO;2

Kaplan J, DeMaria M. 2003. Large-scale characteristics of rapidly intensifying tropical cyclones in the North Atlantic basin. Weather and Forecasting 18: 1093-1108. https://doi.org/10.1175/1520-0434(2003)018<1093:LCORIT>2.0.CO;2

Kaplan J, DeMaria M, Knaff JA. 2010. A revised tropical cyclone rapid intensification index for the Atlantic and eastern North Pacific basins. Weather and Forecasting 25: 220-241. https://doi.org/10.1175/2009WAF2222280.1

Katsube K, Inatsu M. 2016. Response of tropical cyclone tracks to sea surface temperature in the western North Pacific. Journal of Climate 29: 1955-1975. https://doi.org/10.1175/JCLI-D-15-0198.1

Kwon YC, Hong SY. 2017. A mass-flux cumulus parameterization scheme across gray-zone resolutions. Monthly Weather Review 145: 583-598. https://doi.org/10.1175/MWR-D-16-0034.1

Lee CY, Chen SS. 2014. Stable boundary layer and its impact on tropical cyclone structure in a coupled atmosphere-ocean model. *Monthly Weather Review 142*: 1927-1944. https://doi.org/10.1175/MWR-D-13-00122.1

Mahoney KM. 2016. The representation of cumulus convection in high-resolution simulations of the 2013 Colorado front range flood. Monthly Weather Review 144: 4265-4278. https://doi.org/10.1175/MWR-D-16-0211.1

Marras I, Fiori E, Rossi R, Parodi A. 2017. Effects of the representation of convection on the modelling of Hurricane Tomas (2010). Advances in Meteorology 2017: 1762137. https://doi.org/10.1155/2017/1762137

Menemenlis D, Fukumori I, Lee T. 2005. Using Green's functions to calibrate an ocean general circulation model. Monthly Weather Review 133: 1224-1240. https://doi.org/10.1175/MWR2912.1

Menemenlis D, Campin JM Heimbach P, Hill C, Lee T, Nguygen A, Schodlok M, Zhang H. 2008. ECCO2: High-resolution global ocean and sea ice data synthesis. Mercator Ocean Quarterly Newsletter 31: 13-21.

Miller W, Zhang DL. 2019. Understanding the unusual looping track of Hurricane Joaquin (2015) and its forecast errors. Monthly Weather Review 147: 2231-2259. https://doi.org/10.1175/MWR-D-18-0331.1

Miyamoto Y, Bryan GH, Rotunno R. 2017. An analytical model of maximum potential intensity for tropical cyclones incorporating the effect of ocean mixing. Geophysical Research Letters 44: 5826-5835. https://doi.org/10.1002/2017GL073670

Mlawer EJ, Taubman SJ, Brown PD, Iacono MJ, Clough SA. 1997. Radiative transfer for inhomogeneous atmospheres: RRTM, a validated correlated-k model for the longwave. Journal of Geophysical Research: Atmospheres 102: 16663-16682. https://doi.org/10.1029/97JD00237

Mooney PA, Gill DO, Mulligan FJ, Bruyère CL. 2016. Hurricane simulation using different representations of atmosphere-ocean interaction: the case of Irene (2011). Atmospheric Science Letters 17: 415-421. https://doi.org/10.1002/asl.673

NCEP. 2015. NCEP GFS 0.25 Degree global forecast grids historical archive (updated daily) [ds084.1]. Research Data Archive at the National Center for Atmospheric Research, Computational and Information Systems Laboratory. National Centers for Environmental Prediction/National Weather Service/NOAA/U.S. https://doi.org/10.5065/D65D8PWK (accessed 28 October 2023)

Neumann CJ. 1979. On the use of deep-layer mean geopotential height fields in statistical prediction of tropical cyclone motion. In: Sixth Conference on Probability and Statistics in Atmospheric Sciences. American Meteorological Society, Banff, Alta., Canada, 32-38.

NHC. 2023. Hurricane Otis advisory archive. National Hurricane Center. Available at: https://www.nhc.noaa.gov/archive/2023/OTIS.shtml? (accessed 5 November 2023).

Park H, Kim G, Cha DH, Chang EC, Kim J, Park SH, Lee DK. 2022. Effect of a scale-aware convective parameterization scheme on the simulation of convective cells-related heavy rainfall in South Korea. Journal of Advances in Modeling Earth Systems 14: e2021MS002696. https://doi.org/10.1029/2021MS002696

Parker CL, Lynch AH, Mooney PA. 2017. Factors affecting the simulated trajectory and intensification of Tropical Cyclone Yasi (2011). Atmospheric Research 194: 27-42. https://doi.org/10.1016/j.atmosres.2017.04.002

Pollard RT, Rhines PB, Thompson R. 1973. The deepening of the wind-mixed layer. Geophysical Fluid Dynamics 4: 381-404. https://doi.org/10.1080/03091927208236105

Price JF, Weller RA, Pinkel R. 1986. Diurnal cycling: Observations and models of the upper ocean response to diurnal heating, cooling, and wind mixing. Journal of Geophysical Research: Oceans 91: 8411-8427. https://doi.org/10.1029/JC091iC07p08411

Price JF, Sanford TB, Forristall GZ, 1994. Forced stage response to a moving hurricane. Journal of Physical Oceanography 24: 233-260. https://doi.org/10.1175/1520-0485(1994)024<0233:FSRTAM>2.0.CO;2

Reynolds RW, Smith TM, Liu C, Chelton DB, Casey KS, Schlax MG. 2007. Daily high-resolution-blended analyses for sea surface temperature. Journal of Climate 20: 5473-5496. https://doi.org/10.1175/2007JCLI1824.1

Samala BK, C N, Banerjee S, Kaginalkar A, Dalvi M. 2013. Study of the Indian summer monsoon using WRF-ROMS regional coupled model simulations. Atmospheric Science Letters 14: 20-27. https://doi.org/10.1002/asl2.409

Saunders P, Yu Y, Pu Z. 2019. Sensitivity of numerical simulations of Hurricane Joaquin (2015) to cumulus parameterization schemes: Implications for processes controlling a hairpin turn in the track. Journal of the Meteorological Society of Japan Series II 97: 577-595. https://doi.org/10.2151/jmsj.2019-030

Shchepetkin AF, McWilliams JC. 2005. The regional oceanic modeling system (ROMS): A split-explicit, free-surface, topography-following-coordinate oceanic model. Ocean Modelling 9: 347-404. https://doi.org/10.1016/j.ocemod.2004.08.002

Shepherd TJ, Walsh KJ. 2017. Sensitivity of hurricane track to cumulus parameterization schemes in the WRF model for three intense tropical cyclones: Impact of convective asymmetry. Meteorology and Atmospheric Physics 129: 345-374. https://doi.org/10.1007/s00703-016-0472-y

Shu S, Ming J, Chi P. 2012. Large-scale characteristics and probability of rapidly intensifying tropical cyclones in the western North Pacific basin. Weather and Forecasting 27: 411-423. https://doi.org/10.1175/WAF-D-11-00042.1

Singh J, Singh N, Ojha N, Sharma A, Pozzer A, Kiran Kumar N, Rajeev K, Gunte SS, Kotamarthi VR. 2021. Effects of spatial resolution on WRF v. 3.8.1 simulated meteorology over the central Himalaya. Geoscientific Model Development 14: 1427-1443. https://doi.org/10.5194/gmd-14-1427-2021

Skamarock WC, Klemp JB, Dudhia J, Gill DO, Barker D, Duda MG, Huang X-Y, Wang W, Powers JG. 2008. A description of the Advanced Research WRF Version 3 (No. NCAR/TN-475+STR). University Corporation for Atmospheric Research. https://doi.org/10.5065/D68S4MVH

Sun BY, Bi XQ. 2019. Validation for a tropical belt version of WRF: Sensitivity tests on radiation and cumulus convection parameterizations. Atmospheric and Oceanic Science Letters 12: 192-200. https://doi.org/10.1080/16742834.2019.1590118

Tewari M, Chen F, Wang W, Dudhia J, Lemone MA, Mitchell KE, Ek M, Gayno G, Wegiel JW, Cuenca R. 2004. Implementation and verification of the unified Noah land-surface model in the WRF model (presentation). In: 20th Conference on Weather Analysis and Forecasting/16th Conference on Numerical Weather Prediction. American Meteorological Society, Seattle, WA, US.

Tiedtke M. 1989. A comprehensive mass flux scheme for cumulus parameterization in large-scale models. Monthly Weather Review 117: 1779-1800. https://doi.org/10.1175/1520-0493(1989)117<1779:ACMFSF>2.0.CO;2

Torn RD, Davis CA. 2012. The Influence of shallow convection on tropical cyclone track forecasts. Monthly Weather Review 140: 2188-2197. https://doi.org/10.1175/MWR-D-11-00246.1

Torn RD, Elless TJ, Papin PP, Davis CA. 2018. Tropical cyclone track sensitivity in deformation steering flow. Monthly Weather Review 146: 3183-3201. https://doi.org/10.1175/MWR-D-18-0153.1

Trent K. 2007. Simulation of hurricane-ocean interaction for Hurricane Katrina: Coupling WRF with a 1-D ocean model. UCAR-NCAR. https://doi.org/10.5065/dzrr-fx58

Varga ÁJ, Breuer H. 2020. Sensitivity of simulated temperature, precipitation, and global radiation to different WRF configurations over the Carpathian Basin for regional climate applications. Climate Dynamics 55: 2849-2866. https://doi.org/10.1007/s00382-020-05416-x

Wang Y. 2002a. Vortex Rossby waves in a numerically simulated tropical cyclone. Part I: Overall structure, potential vorticity, and kinetic energy budgets. *Journal of the Atmospheric Sciences 59*: 1213-1238. https://doi.org/10.1175/1520-0469(2002)059<1213:VRWIAN>2.0.CO;2

Wang Y. 2002b. Vortex Rossby waves in a numerically simulated tropical cyclone. Part II: The role in tropical cyclone structure and intensity changes. *Journal of the Atmospheric Sciences* 59: 1239-1262. https://doi.org/10.1175/1520-0469(2002)059<1239:VRWIAN>2.0.CO;2

Wang Y, Wu CC. 2004. Current understanding of tropical cyclone structure and intensity changes – A review. Meteorology and Atmospheric Physics 87: 257-278. https://doi.org/10.1007/s00703-003-0055-6

Wang Y, Rao Y, Tan ZM, Schönemann D. 2015. A Statistical analysis of the effects of vertical wind shear on tropical cyclone intensity change over the western North Pacific. Monthly Weather Review 143: 3434-3453. https://doi.org/10.1175/MWR-D-15-0049.1

Wong MLM, Chan JCL, Zhou W. 2008. A simple empirical model for estimating the intensity change of tropical cyclones after landfall along the South China coast. *Journal of Applied Meteorology and Climatology 47*: 326-338. https://doi.org/10.1175/2007JAMC1633.1

Wu CC, Emanuel KA. 1993. Interaction of a baroclinic vortex with background shear: Application to hurricane movement. *Journal of Atmospheric Sciences 50*: 62-76. https://doi.org/10.1175/1520-0469(1993)050<0062:IOABVW>2.0.CO;2

Yang B, Zhang Y, Qian Y, Wu T, Huang A, Fang Y. 2015. Parametric sensitivity analysis for the Asian Summer Monsoon precipitation simulation in the Beijing Climate Center AGCM, Version 2.1. *Journal of Climate 28*: 5622-5644. https://doi.org/10.1175/JCLI-D-14-00655.1

Yao MS, del Genio AD. 1999. Effects of cloud parameterization on the simulation of climate changes in the GISS GCM. *Journal of Climate 12:* 761-779. https://doi.org/10.1175/1520-0442(1999)012<0761:EOCPOT>2.0.CO;2

Zhang C, Wang Y, Hamilton K. 2011. Improved representation of boundary layer clouds over the Southeast Pacific in ARW-WRF using a modified Tiedtke cumulus parameterization scheme. *Monthly Weather Review 139*: 3489-3513. https://doi.org/10.1175/MWR-D-10-05091.1

Zhang F, Li M, Ross AC, Lee SB, Zhang D. 2017. Sensitivity analysis of Hurricane Arthur (2014) storm surge forecasts to WRF physics parameterizations and model configurations. *Weather and Forecasting 32*: 1745-1764. https://doi.org/10.1175/WAF-D-16-0218.1

Zheng Y, Alapaty K, Herwehe JA, Del Genio AD, Niyogi D. 2016. Improving high-resolution weather forecasts using the Weather Research and Forecasting (WRF) model with an updated Kain-Fritsch scheme. *Monthly Weather Review 144*: 833-860. https://doi.org/10.1175/MWR-D-15-0005.1

SUPPLEMENTARY MATERIAL

Table SI. Summary of the ATMOS experiments.

Experiment name	Minimum MSLP		Landfall on October 25				
	MSLP	FT	MSLP	FT	UT	TD	DD
GFS_KF-0_15KM	957.98	71	NA	NA	NA	NA	NA
ERA5_GF-0_15KM	973.04	69	NA	NA	NA	NA	NA
ERA5_KF-0_15KM	967.76	48	989.85	60	12	+6	64.84
ERA5_KF-2_15KM	965.58	48	989.98	61	13	+7	95.08
ERA5_GF-0_10KM	973.92	60	NA	NA	NA	NA	NA
ERA5_TK-0_10KM_DT30	975.89	60	NA	NA	NA	NA	NA
ERA5_TK-2_10KM_DT30	977.9	57	NA	NA	NA	NA	NA
ERA5_MSKF-0_10KM_DT30	976.36	53	NA	NA	NA	NA	NA
ERA5_MSKF-2_10KM_DT30	971.25	46	NA	NA	NA	NA	NA
ERA5_KF-0_10KM_DT60_CUDT5	968.94	47	991.48	59	11	+5	70.57
ERA5_KF-0_10KM_DT30_CUDT5	967.27	46	989.56	58	10	+4	74.42
ERA5_KF-0_10KM_DT30_CUDT0	970.91	45	988.45	56	8	+2	47.73
ERA5_KF-2_10KM_DT60_CUDT5	962.6	46	987.76	60	12	+6	74.42
ERA5_KF-2_10KM_DT30_CUDT5	959.1	47	984.94	58	10	+4	74.42
ERA5_KF-2_10KM_DT30_CUDT0	967.04	46	989.69	58	10	+4	83.91
ERA5_KF-0_5KM_CUDT0	960.73	45	983.29	54	6	+0	39.59
ERA5_WSM6-0_5KM	975.33	55	NA	NA	NA	NA	NA
ERA5_GF-0_5KM	970.10	49	NA	NA	NA	NA	NA
ERA5_MSKF-0_5KM	973.91	50	NA	NA	NA	NA	NA

MSLP: mean sea level pressure; FT: forecast time; UT: UTC time; TD: time difference; DD: distance difference.

Table SII. Summary of the COUPLED experiments. .

Experiment name	Minimum MSLP		Landfall on October 25				
	MSLP	FT	MSLP	FT	UT	TD	DD
ERA5_KF-0_15KM_CUDT5	972.38	48	1002.03	65	17	+11	114.1
ERA5_KF-0_15KM_HOM.T_CUDT5	971.4	44	993.43	61	13	+7	64.84
ERA5_KF-0_10KM_CUDT5	962.94	48	992.49	60	12	+6	107.08
ERA5_KF-0_10KM_HOM.T_CUDT5	963.28	48	989.59	58	10	+4	65.2
ERA5_KF-0_10KM_HOM.TS_CUDT5	959.21	47	986.36	57	9	+3	57.88
ERA5_KF-0_10KM_HOM.TS_CUDT0	960.89	47	983.02	56	8	+2	46.38
OISST_0.50_KF-0_10KM_CUDT5	969.93	48	991.88	59	11	+5	88.39
OISST_0.50_KF-0_10KM_HOM.T_CUDT5	968.14	45	986.18	57	9	+3	60.77
OISST_0.50_KF-0_10KM_HOM.TS_CUDT5	964.68	45	984.9	57	9	+3	60.77
OISST_0.25_KF-0_10KM_CUDT5	966.04	47	989.5	59	11	+5	93.59
OISST_0.25_KF-0_10KM_HOM.TS_CUDT5	962.51	46	984.03	57	9	+3	60.77
OISST_0.25_KF-0_10KM_HOM.TS_CUDT0	963.98	46	986.06	56	8	+2	37.71
OISST_0.25_KF-2_10KM_HOM.TS_CUDT0	962.33	46	986.33	56	8	+2	74.42
OISST_0.25_KF-0_5KM_HOM.TS_CUDT0	961.9	46	983.79	53	5	–1	39.59

MSLP: mean sea level pressure; FT: forecast time; UT: UTC time; TD: time difference; DD: distance difference.

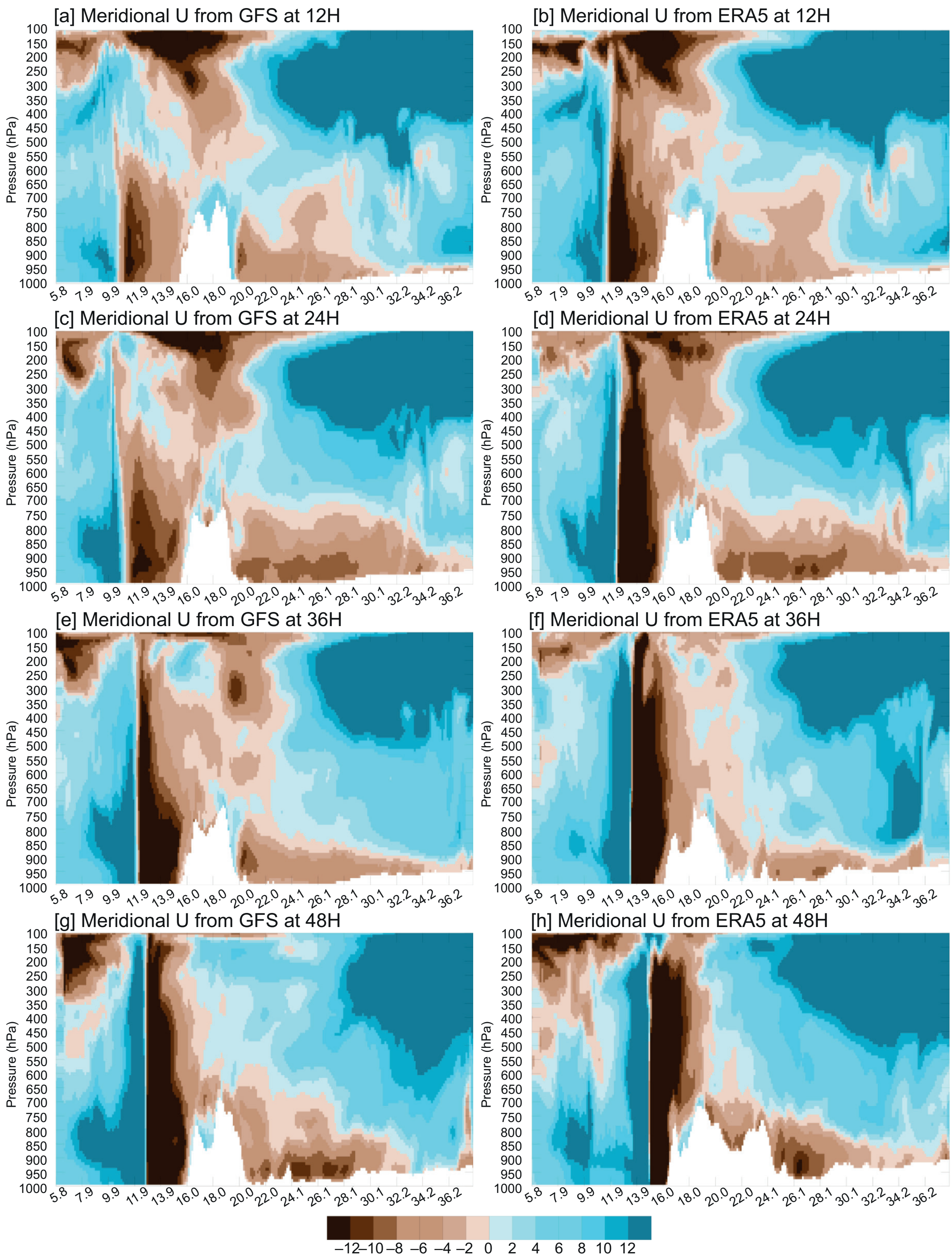

Fig. S1. Cross-section of the wind U component concerning the simulated position at hours 12, 24, 36, and 48. The first column corresponds to the ATMOS_GFS_KF-0 experiment, and the second corresponds to the ATMOS_ERA5_KF-0 experiment.

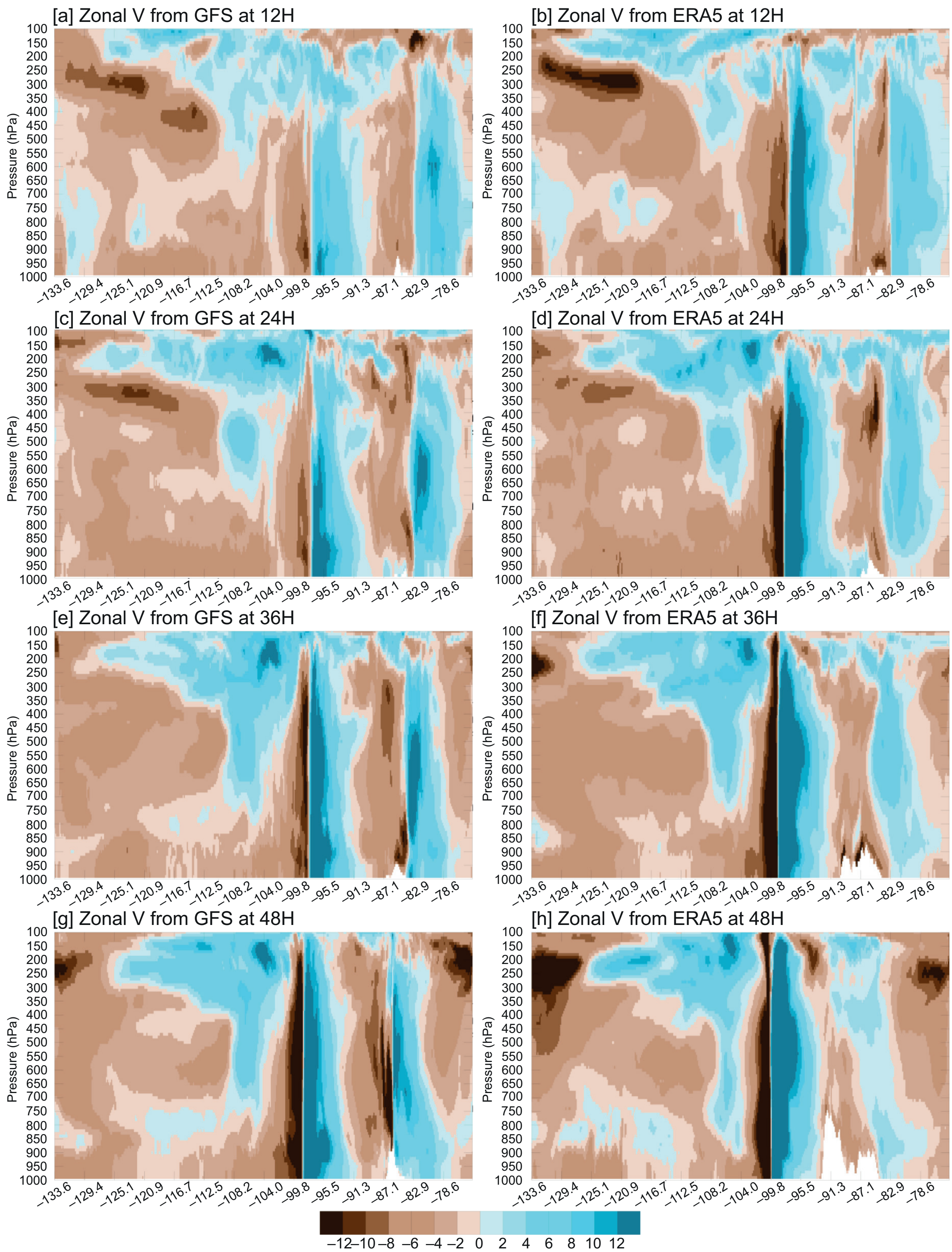

Fig. S2. Cross-section of the wind V component concerning the simulated position at hours 12, 24, 36, and 48. The first column corresponds to the ATMOS_GFS_KF-0 experiment, and the second corresponds to the ATMOS_ERA5_KF-0 experiment.

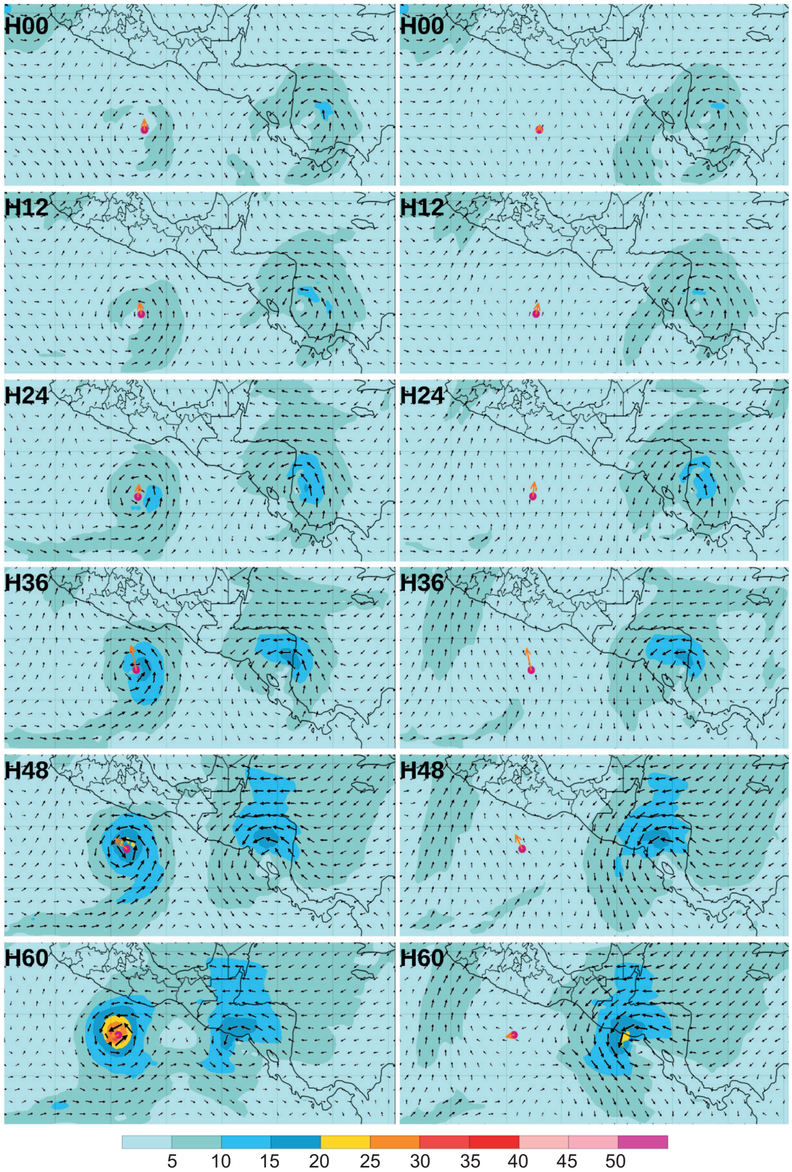

Fig. S3. Wind maps averaged between 850 and 500 hPa from the experiment ATMOS_GFS_KF-0_15KM. The colors indicate wind speed in km h^{-1}. Pink dots indicate the simulated surface position of the HO, and arrows indicate the direction of the average wind or ESF, within a 3º radius. The first column corresponds to the simulated average field (without removing the storm), and the second corresponds to the ESF.

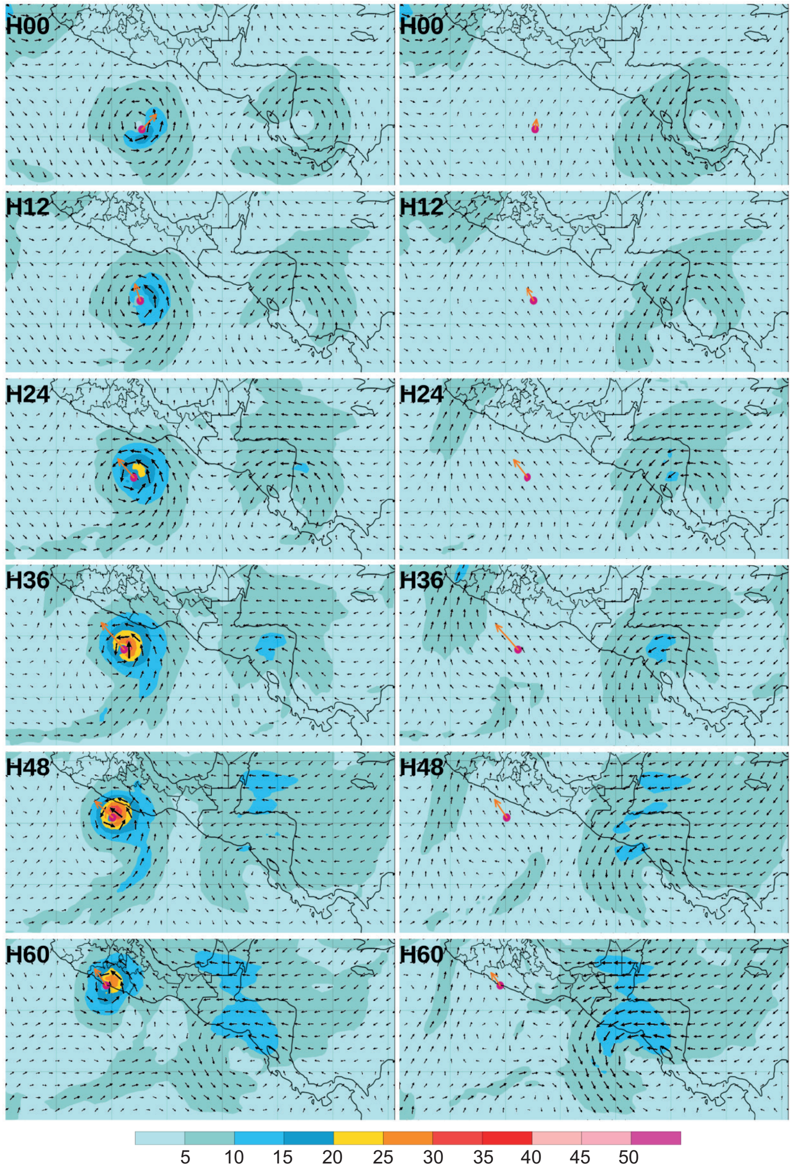

Fig. S4. Wind maps averaged between 850 and 500 hPa from the experiment ATMOS_ERA5_KF-0_15KM. The colors indicate wind speed in km h^{-1}. Pink dots indicate the simulated surface position of the HO, and arrows indicate the direction of the average wind or ESF, within a 3º radius. The first column corresponds to the simulated average field (without removing the storm), and the second corresponds to the ESF.

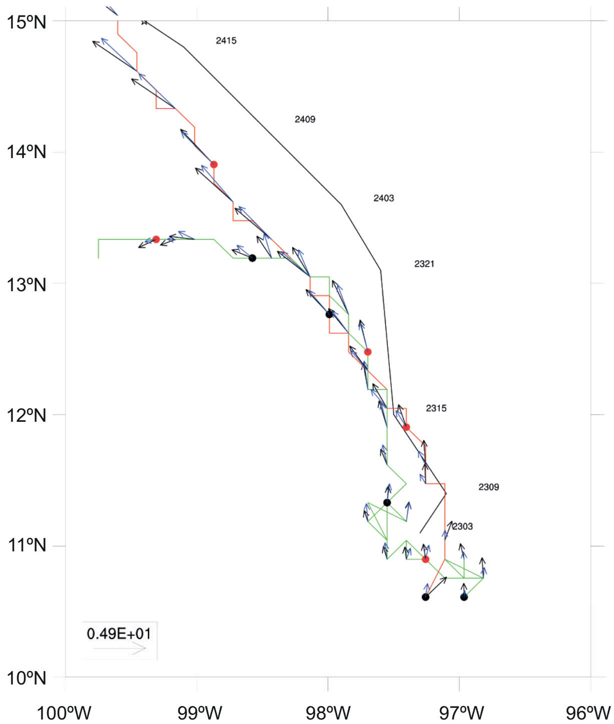

Fig. S5. ESF averaged between 850 and 500 hPa within a 3º radius around the simulated storm center. Black arrows represent the average wind values (before storm removal), and blue arrows represent the environmental steering flow. Arrows orientation and length indicate the direction and magnitude, respectively. The black line corresponds to the trajectory of HO according to the PA; the green line corresponds to the ATMOS_GFS_KF-0_15KM experiment, and the red line to ATMOS_ERA5_KF-0_15KM.

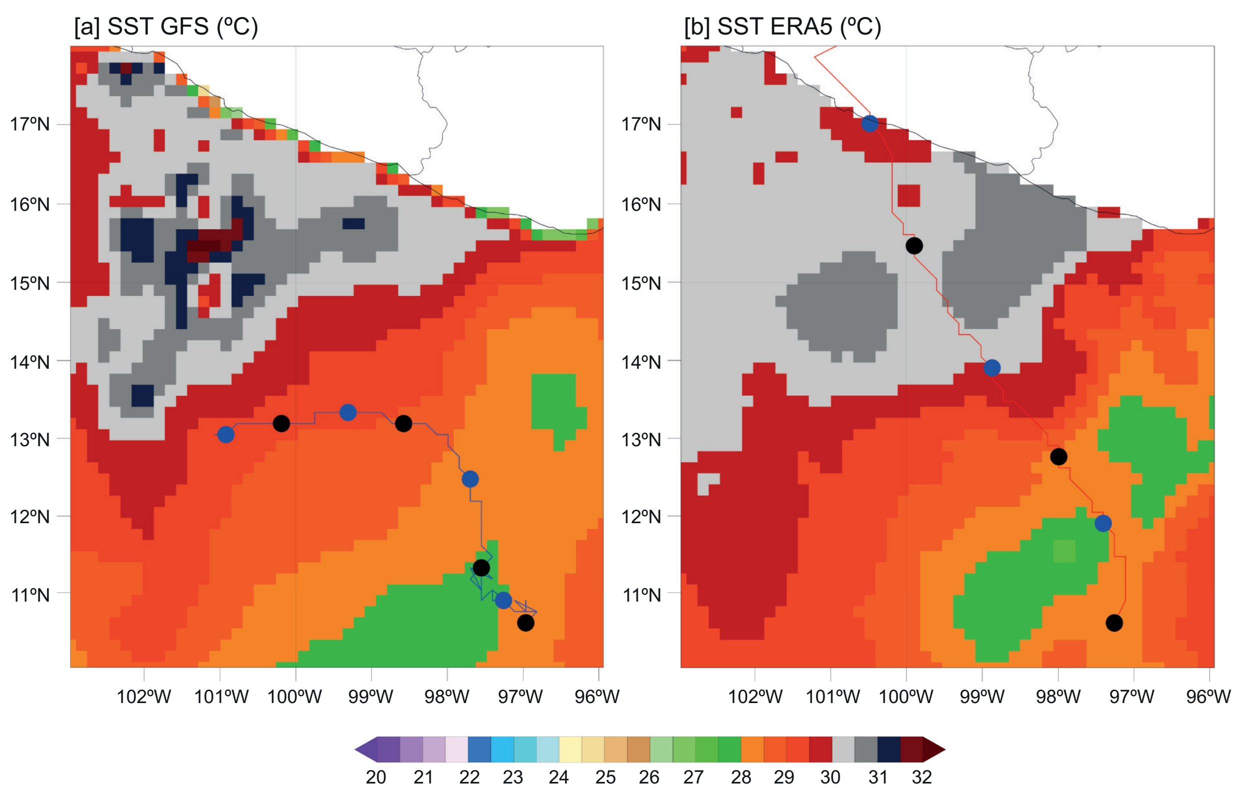

Fig. S6. Simulated trajectories over the SST fields of each experiment. (a) ATMOS_GFS_KF-0_15KM, (b) ATMOS_ERA5_KF-0_15KM.